Geophys. J. Int. (2008) **172,** 311–330 doi: 10.1111/j.1365-246X.2007.03632.x

Wave-equation shear wave splitting tomography

Maureen D. Long,[1,*] Maarten V. de Hoop[2] and Robert D. van der Hilst[1]

[1]*Department of Earth, Atmospheric, and Planetary Sciences, Massachusetts Institute of Technology,* 77 *Massachusetts Ave., Cambridge,* MA 02139, *USA. E-mail: mlong@alum.mit.edu*

[2]*Center for Computational and Applied Mathematics, Purdue University,* 150 N. *University St., West Lafayette,* IN 47907, *USA*

Accepted 2007 September 23. Received 2007 September 22; in original form 2007 May 7

SUMMARY

The main focus of this paper is the development of a theoretical framework for the tomographic inversion of (broad-band) shear wave splitting measurements in terms of anisotropic structure in the upper mantle. We show that the partial differential equations (PDEs) that govern wave equation shear wave splitting tomography are, upon linearization with the Born approximation, similar in structure to the equations that describe wave equation transmission and reflection tomography. For full broad-band analysis these PDEs can be evaluated numerically, but we show here the leading order asymptotic (i.e. 'ray born') behaviour of the associated finite-frequency sensitivity kernels. For simplicity we assume that the anisotropic model is invariant in one horizontal direction. This 2.5-D geometry is well suited for studying upper-mantle anisotropy associated with subduction of lithospheric plates if the trench-slab system is approximately 2-D. With the so-called splitting intensity as the metric for data fit, and under the assumption of weak anisotropy, we derive expressions for the sensitivity kernels. We focus on two anisotropic parameters that describe tilted transverse isotropy: the dip θ_0 of the symmetry axis with respect to the horizontal plane and the anellipticity parameter ϵ_{A}, which represents the strength of the anisotropy. We illustrate the finite-frequency effects both for homogeneous and heterogeneous (anisotropic) background models. The sensitivity kernels in heterogeneous media are calculated for initial models obtained from numerical modelling of flow and finite strain beneath the Ryukyu arc. Kernels calculated in heterogeneous media differ substantially from those in a homogeneous background. This demonstrates the importance of iterative model (and kernel) assessment for reaching the full (resolution) potential of finite frequency tomography.

Key words: Seismic anisotropy; Seismic tomography; Theoretical seismology.

1 INTRODUCTION

Since the pioneering work by Hess (1964), measurements of seismic anisotropy in the upper mantle have provided information on the geometry of deformation associated with tectonic and geodynamic processes. Seismic anisotropy in the upper mantle is generally understood to arise when an aggregate of mantle rock, composed of intrinsically anisotropic crystals (for instance, olivine) is subjected to strain and develops a lattice preferred orientation, or LPO (e.g. Christensen 1984; Zhang & Karato 1995). Vice versa, measurement of anisotropy provides insight into the geometry of deformation and flow in Earth's interior. An unambiguous indicator of anisotropy, the splitting—or birefringence—of shear waves (Kosarev *et al.* 1979; Ando *et al.* 1983; Fukao 1984) provides unique insight into the structure and deformation of the upper mantle (e.g. Silver 1996; Savage 1999) and, for instance, into mantle flow patterns associated with the subduction of oceanic lithosphere (e.g. Park & Levin 2002).

Shear wave splitting has provided strong evidence for anisotropy in subduction zones (e.g. Fouch & Fischer 1996; Fischer *et al.* 1998; Smith *et al.* 2001; Anderson *et al.* 2004; Pozgay *et al.* 2007). However, many of the measurements used lack depth resolution because the pertinent waves propagate nearly vertically through the upper mantle. The prevailing stress and temperature conditions and the presence of water (and perhaps other volatiles) can have a profound effect on anisotropic fabric (Jung & Karato 2001; Mizukami *et al.* 2004; Skemer *et al.* 2006). For instance, in B-type olivine fabric the fast axis is oriented $\sim 90^\circ$ from the prevailing flow direction (Jung & Karato 2001; Karato 2003; Kneller *et al.* 2005; Lassak *et al.* 2006). Moreover, the commonly used assumption of infinite strain (and, thus, the neglect of strain

*Now at: Department of Terrestrial Magnetism, Carnegie Institution of Washington, 5241 Broad Branch Road, NW, Washington, DC 20015, USA.

history) may not always be adequate (Kaminski & Ribe 2002). Consequently, interpretations of splitting measurements are non-unique and not often uncontroversial (e.g. Park & Levin 2002; Wiens & Smith 2003).

Insight into the 2-D or 3-D distribution of strain in the mantle wedge can be obtained by comparing predictions from geodynamic models with splitting observations (e.g. Hall *et al.* 2000; Long *et al.* 2007). However, the inability to explore the full parameter space can easily introduce bias. Alternatively, (tomographic) inversion of shear wave splitting data sets, which is becoming feasible thanks to the increasing availability of data from dense, long-running seismic arrays, can elucidate aspects of mantle deformation in complicated tectonic regions such as subduction zones.

In exploration seismology, splitting data from vertical seismic profiling (e.g. Esmersoy 1990; MacBeth 1991) or shear wave polarization and traveltimes (Zheng 2004; Yang *et al.* 2005) have been used to invert for anisotropic parameters. Šílený & Plomerová (1996) inferred anisotropy of continental lithosphere from inversion of shear wave splitting parameters and *P*-wave traveltime residuals, and Ryberg *et al.* (2005) inverted shear wave splitting measurements for single *SKS* arrivals across a dense receiver array using a coarse block model and a parameter space search method. Tomographic inversion for anisotropic parameters faces several challenges, however. First, one needs seismograph networks (or geophone arrays) that allow dense sampling of the three-component wavefield and with favourable locations with respect to seismic sources in order to obtain sampling from a sufficiently large range of backazimuths and incidence angles. Second, the problem of inverting for laterally varying general anisotropy (defined by 21 independent elastic parameters) is ill posed (e.g. De Hoop *et al.* 1999; Foss *et al.* 2005).

In our shear wave splitting tomography we address data coverage and non-uniqueness as follows. First, we use a permanent, dense broad-band seismic array (the Japanese *F*-net array; see Long & Van der Hilst 2005a) to construct a large database of high-quality shear wave splitting measurements with good ray coverage in the upper mantle. Second, we reduce the complexity of the problem by assuming that the anisotropic structure is invariant in the direction of the strike of the trench. This strategy is adequate for studies of anisotropy in nearly 2-D systems, such as the Ryukyu subduction zone. Indeed, Long and Van der Hilst (2006) concluded that trench-perpendicular corner flow along the Ryukyu arc is consistent with their splitting observations. In this 2.5-D geometry we collapse the stations and ray paths to and constrain anisotropy in a 2-D plane of symmetry. Third, we use results from geodynamic flow modelling (Long *et al.* 2007) to regularize the inversion problem. Specifically, we use a 2-D anisotropic reference model that is consistent with the splitting observations as a starting point for the computation of sensitivity kernels. Such kernels will be used for tomographic inversion of the measurements by Long & Van der Hilst (2005a), with the objective of constraining upper-mantle anisotropy and upper-mantle flow beneath Ryukyu and southwestern Japan (Long *et al.* in preparation).

Here, we develop the theory up to the calculation of wave equation sensitivity kernels for (2.5-D) shear wave splitting tomography and a table of symbols used in the derivations below is given in Appendix A. We use the so-called 'splitting intensity' (Chevrot 2000, 2006) as the data misfit criterion. Linearization (through the Born approximation) then leads to a system of partial differential equations (PDEs) associated with full-wave propagation, the solution of which generates the sensitivity kernel. The structure of this system follows an adjoint state method, and resembles the structure appearing in wave equation transmission and reflection tomography (De Hoop & Van der Hilst 2005a; Tromp *et al.* 2005; De Hoop *et al.* 2006). The PDEs can be solved numerically to obtain full-wave kernels in 3-D, but here we analyse the leading order (asymptotic) behaviour using anisotropic ray perturbation theory (e.g. Farra 1989, 2001; Jech & Pšenčík 1989) in 2.5-D.

In this paper, we introduce full-wave equation-based splitting intensity kernels. The asymptotic expansion of these kernels has many similarities with the analysis of Favier & Chevrot (2003), Chevrot *et al.* (2004) and Chevrot (2006), but there are also important differences. First, in our asymptotic approach we choose a parametrization scheme that is explicitly designed to study anisotropy in subduction zones and which builds on results from modelling (Long *et al.* 2007). Secondly, we reduce the geometry to 2.5-D by assuming invariance in one direction (along strike) and wave propagation in or near a great circle plane of symmetry. Finally, recognizing that full resolution and accurate imaging can only be achieved when kernels are adapted to the heterogeneity under study (De Hoop & Van der Hilst 2005a; De Hoop *et al*. 2006), and in view of the concept of using flow models to regularize the tomographic inversions, we focus on computing sensitivity kernels for heterogeneous, anisotropic background media. We show that kernels in a heterogeneous anisotropic background can appear very different from kernels calculated in a homogeneous medium, which suggests that the latter may lead to a false sense of image improvement. In Appendix B, we compare our asymptotic formulation with kernels developed by Favier & Chevrot (2003) and show that for a homogeneous, isotropic reference medium they are equivalent.

2 THE CROSS-CORRELATION SPLITTING INTENSITY CRITERION

Shear wave splitting is most often measured using grid search methods that seek to 'remove' or compensate for the effect of splitting from a single measurement of an incoming shear wave. Methods that seek to remove the energy on the transverse component of the seismogram (e.g. Silver & Chan 1988, 1991) or to maximize the similarity in the pulse shapes of the fast and slow arrivals (e.g. Bowman & Ando 1987; Levin *et al.* 1999) are commonly used. Chevrot (2000) introduced a quantity known as the 'splitting intensity' that is sensitive to the 'relative' energy on the transverse component of the seismogram. For the simple case of a single layer of anisotropy, the splitting intensity varies with incoming polarization angle θ with a $\sin(2\beta)$ dependence, where β is the angle between θ and the fast direction ϕ. The fast direction ϕ and split time δt of the layer are retrieved from the amplitude and phase of the sinusoid (see Appendix B). For the case of more complicated anisotropy, which can potentially be resolved by tomography, the splitting intensity will have a more complicated pattern

but remains a convenient observable with which to work. Indeed, for the tomographic problem the splitting intensity has several advantages over 'apparent' or 'effective' measurements of $(\phi, \delta t)$ in complicated media. First, splitting intensity is a more robust measurement (Chevrot 2000; Long & Van der Hilst 2005b). Second, near-zero splitting is more easily measured and distinguished from so-called 'null measurements' (which may include genuine zero splitting as well as failed measurement attempts). Third, splitting intensity is commutative, in contrast to the so-called splitting operator $\mathbf{\Gamma^{-1}}$ (Silver & Savage 1994), which means that it can be treated very much like, for example, a traveltime delay in wave speed tomography.

For the purpose of defining the cross-correlation splitting intensity criterion, we first define the geometry of the polarizations of the incoming shear wave (see Fig. 1). We define the radial component direction to coincide with the initial polarization direction of the shear wave, before it is affected by upper-mantle anisotropy, and assume that the shear wave is initially (linearly) SV polarized. The transverse component direction is orthogonal to the radial direction in the horizontal plane. The radial and transverse component geometry is intrinsically controlled by the source and receiver geometry [for $SK(K)S$] and, for direct teleseismic S arrivals, by the geometry of the earthquake source; this coordinate system is independent of the geometry of the anisotropic medium and follows that of (Chevrot 2000, 2006).

Sensitivity kernels for finite frequency tomography depend on the way the data are characterized and analysed (e.g. De Hoop & Van der Hilst 2005a). A popular choice is the cross-correlation criterion (e.g. Luo and Schuster 1991; Dahlen *et al*. 2000). The splitting detection criterion used here, the splitting intensity measurement, is derived from the cross-correlation criterion, but instead of comparing for each event, at any given station, modelled data with observed data, we compare the radial (superscript ^{R}) component (essentially the projection onto an effective qSV polarization) with the transverse (superscript ^{T}) component (essentially the projection onto an effective qSH polarization) of the observed trace u. The similarity between the splitting intensity and the traveltime delay obtained by cross-correlation was also discussed by Chevrot (2006). In this context, we consider $\partial_t C(u^R, u^T)(t)$, where C stands for time-domain cross-correlation, that is, $\mathrm{C}(u^R, u^T)(t) = \int u(t+t')^R u(t')^T dt'$.

As in most other studies of teleseismic shear wave splitting due to upper-mantle anisotropy (e.g. Silver & Chan 1988, 1991; Savage 1999), we assume that the split time $|\delta t|$ is smaller than approximately half the dominant period, say T_0, in the data. This leads to the introduction of the (normalized) splitting intensity measure (Chevrot 2000)

$$\mathrm{S}(\mathbf{x}^s, \mathbf{x}^r) = -N_{s,r}^{-1} \partial_t \mathrm{C}[u(\mathbf{x}^r, .; \mathbf{x}^s)^R, u(\mathbf{x}^r, .; \mathbf{x}^s)^T](0) \tag{1}$$

for a given source–receiver pair $(\mathbf{x}^s, \mathbf{x}^r)$, in which the normalization factor,

$$N_{s,r} = \int \left| \partial_t u(\mathbf{x}^r, t; \mathbf{x}^s)^R \right|^2 \mathrm{d}t, \tag{2}$$

represents the radial component energy. The splitting intensity measure vanishes in the absence of anisotropy.[1]

3 ADJOINT STATE: PDE FORMULATION

We linearize the tomographic problem (locally) using the Born approximation. For this purpose we consider an unperturbed field u_0 (in a smooth, isotropic background medium) and a perturbed field δu (accounting for the presence of anisotropy) and model the multicomponent data as $u = u_0 + \delta u$. Correspondingly, the medium parameters are represented by a sum of a smooth background (c_{ijkl}) and, in the mantle volume under study, a smooth perturbation (δc_{ijkl}). This formulation is valid if the anisotropy is weak (Thomsen 1986) and if all anisotropy can be described by a perturbation δc_{ijkl} of the elasticity tensor. The field u_0 is assumed to be (initially) SV polarized; we denote the associated polarization vector by ${}^R h_0$. The SH polarization vector is denoted by ${}^T h_0$ (with ${}^T h_0 \perp {}^R h_0$).

The aim is to find a sensitivity kernel $\mathcal{K}$ that relates a model perturbation $\delta \mathbf{c} = \delta c_{ijkl}$ at $\boldsymbol{x}$ to the splitting intensity data, S, observed at $\boldsymbol{x}^r$, for sources at $\boldsymbol{x}^s$:

$$\mathrm{S}(\mathbf{x}^s, \mathbf{x}^r) = \int \mathcal{K}(\mathbf{x}^s, \mathbf{x}^r; \mathbf{x}) \delta \mathbf{c}(\mathbf{x})\, \mathrm{d}\mathbf{x} = \int \mathcal{K}_{ijkl}(\mathbf{x}^s, \mathbf{x}^r; \mathbf{x}) \delta c_{ijkl}(\mathbf{x}) \mathrm{d}\mathbf{x}. \tag{3}$$

With our tomography we aim to constrain spatial variations in anisotropic elastic parameters in a localized upper-mantle region beneath the seismograph stations, and we assume background properties (that is, isotropy) everywhere else. Since the (teleseismic) sources are far away from the anisotropic target region, the radial and transverse components of the observed field u can be assumed to be (asymptotically) close to the radial component of (unperturbed) u_0 and the transverse component of (perturbed) δu, respectively. That is, $u_0(\mathbf{x}^r, t; \mathbf{x}^s)^T = {}^T h_{0,i}(\mathbf{x}^r) u_{0,i}(\mathbf{x}^r, t; \mathbf{x}^s) = 0$ (asymptotically). Then, with $\delta u(\mathbf{x}^r, t; \mathbf{x}^s)^T = {}^T h_{0,i}(\mathbf{x}^r) \delta u_i(\mathbf{x}^r, t; \mathbf{x}^s)$, we get

$$\partial_t \mathrm{C}(u^R, u^T)(t) \simeq \partial_t \mathrm{C}\big[u_0^R, (\delta u)^T\big](t). \tag{4}$$

Through the Born approximation for δu, the perturbation to the transverse component $(\delta u)^T$ can be obtained by a linear operator acting on the model perturbation $\delta \mathbf{c} = \delta c_{ijkl}$. Thus, there exists a linear operator H such that:

$$H \delta \mathbf{c} = -\partial_t \mathrm{C}\big(u_0^R, (\delta u)^T\big)(0). \tag{5}$$

[1] Because of the normalization with $N_{s,r}$ the splitting intensity criterion does not quite reproduce the leading-order expansion of $\partial_t C(u^R, u^T)\,(\delta t) = 0$ about zero time lag (corresponding with isotropy).

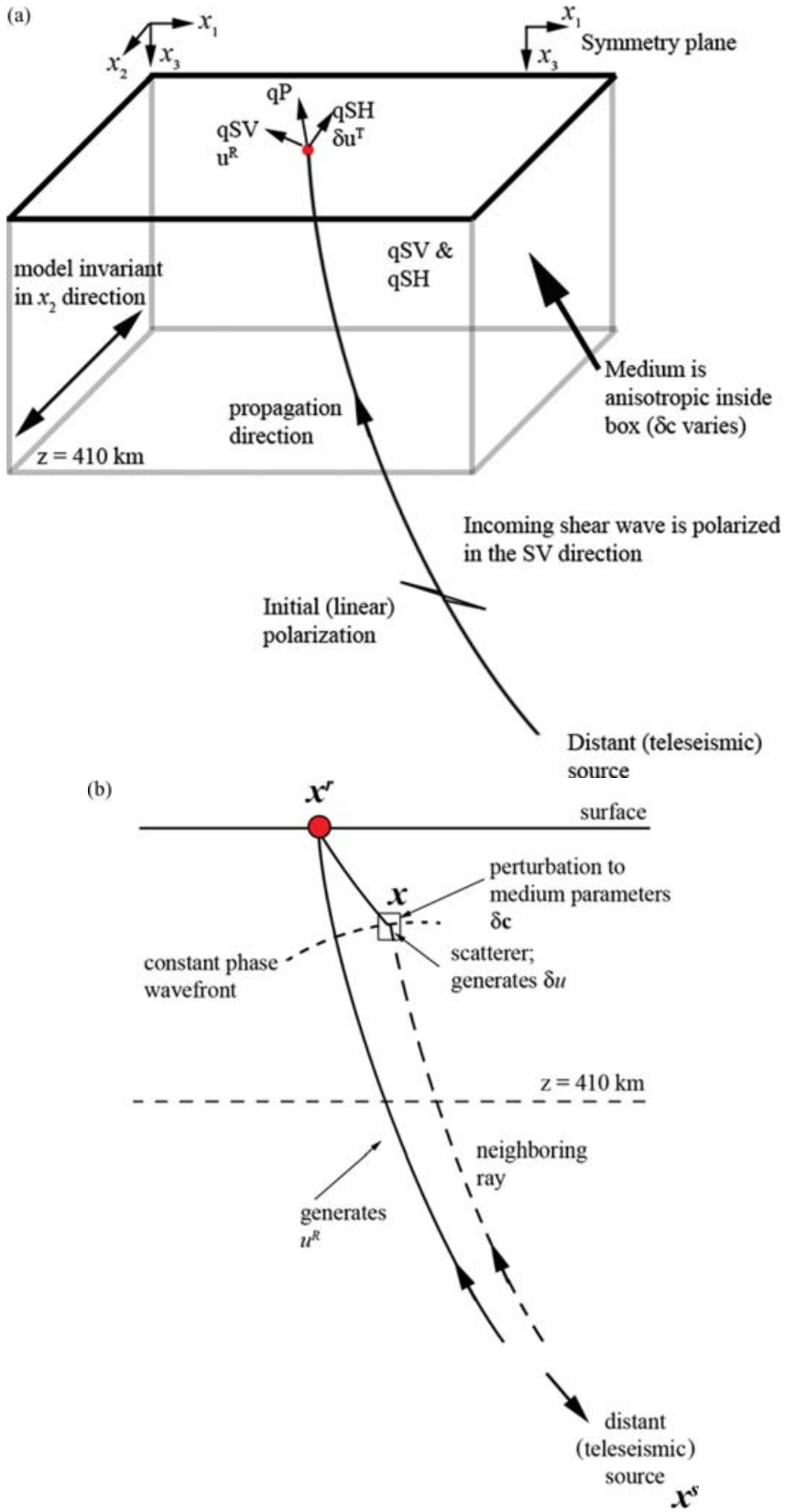

Figure 1. (a) Geometry of the problem setup. The coordinates are chosen so that the anisotropic model is invariant in one horizontal direction (x_2). The medium is considered to be anisotropic above the 410 km discontinuity and isotropic everywhere else. We denote the polarization direction of the initially polarized shear wave (that is, before the influence of anisotropy) as the 'radial' direction. We consider the incoming shear wave to be *SV* polarized; therefore, the radial component of the seismogram records the q-SV energy. The (horizontal) direction orthogonal to 'radial' is the 'transverse' component. The quasi-*SH* energy observed on the transverse component (δu^T) arises solely from the anisotropic perturbation $\delta\mathbf{c}$. (b) Schematic diagram of the sensitivity kernel computation. The sensitivity is computed with respect to the starting model at each scattering point **x**.

We now define a linear (forward) modelling operator $F = \tilde{N}_{s,r}^{-1} H$, with $\tilde{N}_{s,r} = \int |\partial_t u_0^R|^2 \mathrm{d}t$, that operates on $\delta\mathbf{c}$ to give S:

$$\mathrm{S} = F\delta\mathbf{c}. \tag{6}$$

The kernel of linear operator F is the sensitivity kernel $\mathcal{K}$, introduced above in (3). Then, with F^* the adjoint of F, the image of the elasticity tensor update is given by

$$\mathbf{I} = F^*\mathrm{S}. \tag{7}$$

NB. The misfit functional ϵ that expresses the misfit between the forward model and the splitting intensity observations can be defined as $\varepsilon = \frac{1}{2}\iint |\mathrm{S} - F\delta\mathbf{c}|^2 \,\mathrm{d}\mathbf{x}^s \mathrm{d}\mathbf{x}^r$. Various optimization strategies can be employed to minimize this functional, but many have the evaluation of (7) in common.

Using the elastic wave equation, and an adjoint state formulation, the image $\mathbf{I}$ can be obtained through integration of the cross-correlations over all sources:

$$I_{ijkl}(\mathbf{x}) = \int\int \partial_{x_j} w_i^*(\mathbf{x}, -t; \mathbf{x}^s)\partial_{x_l} u_{0,k}(\mathbf{x}, t; \mathbf{x}^s)\,\mathrm{d}t\,\mathrm{d}\mathbf{x}^s, \tag{8}$$

which follows from the solutions of the following inhomogeneous PDEs

$$\begin{aligned}
&\left[\rho(\mathbf{x})\partial_t^2\delta_{ik} - \partial_{x_j} c_{ijkl}(\mathbf{x})\partial_{x_l}\right] u_{0,k}(\mathbf{x}, t; \mathbf{x}^s) = f_i^s(\mathbf{x}, t)\\
&\left[\rho(\mathbf{x})\partial_t^2\delta_{ik} - \partial_{x_j} c_{ijkl}(\mathbf{x})\partial_{x_l}\right] w_k^*(\mathbf{x}, t; \mathbf{x}^s) = \int \tilde{N}_{s,r}^{-1}\mathrm{S}(\mathbf{x}^s, \mathbf{x}^r)^T h_{0,i}(\mathbf{x}^r)\partial_t u_0(\mathbf{x}^r, -t; \mathbf{x}^s)^R \delta(\mathbf{x}^r - \mathbf{x}) d\mathbf{x}^r,
\end{aligned} \tag{9}$$

subjected to zero initial conditions, and with the equivalent body forces $f^s(\mathbf{x}, t)$ given by

$$f_j^s(\mathbf{x}, t) = -M_{ij}(\mathbf{x}^s)\partial_i\delta(\mathbf{x} - \mathbf{x}^s)H(t - t^s), \quad \text{with } t^s = 0 \tag{10}$$

(assuming the far field approximation). Here, M_{ij} represents the moment tensor and H the Heaviside function. In (9), $-t$ reveals a time reversal.[2] The sensitivity kernel is obtained in a manner similar to (8), with the source (right-hand side) of adjoint eq. (9) replaced by $\tilde{N}_{s,r}^{-1T} h_{0,i}(\mathbf{x}^r)\partial_t u_0(\mathbf{x}^r, -t; \mathbf{x}^s)^R \delta(\mathbf{x}^r - \mathbf{x})$ and omitting the integration over $\mathbf{x}^s$. A structure similar to (9) also appears in the PDEs for wave equation transmission and reflection tomography (De Hoop & Van der Hilst 2005a; De Hoop *et al*. 2006), suggesting the existence of a common PDE framework for wave equation tomography.

So far, we have derived the form of the PDEs that govern splitting intensity tomography and from which an image I_{ijkl} of the elastic perturbations (i.e. the anisotropic structure beneath the stations) can be obtained. In the next sections, we derive expressions for the leading-order form of the sensitivity kernel $\mathcal{K}$, defined in eq. (3).

4 PERTURBATION IN 2.5-D AND HIGH-FREQUENCY ASYMPTOTICS

The full-wave sensitivity kernels can be obtained by solving the PDEs in (9) numerically. To explore the leading order effects, however, we develop here an asymptotic representation. Furthermore, even though there is no formal obstruction to extend the analysis to full 3-D, we assume here that the anisotropic model is invariant in one horizontal direction, say x_2, and that we can describe the anisotropy in a 2-D plane of symmetry (x_1, x_3) (see Fig. 2). The station coordinate is then simply the distance from the trench measured in the x_1 direction.

Such a 2.5-D approximation, the treatment of which is more subtle than the 3-D case, is appropriate for the analysis of the tectonic problem under study (a subduction zone whose geometry is well described in 2-D). It reduces the complexity of a severely ill-determined problem and enables the regularization of the tomographic inversion using the results of our 2-D flow simulations (Long *et al.* 2007). Furthermore, collapsing the station geometry (and associated path coverage) onto a 2-D plane dramatically improves the resolution of our tomographic images.

In this section, we derive expressions for the pertinent Green's functions (Section 4.1), their projections onto the 2-D symmetry plane (Section 4.2), the perturbed wavefields (Section 4.3), the medium perturbations (Section 4.4) and—finally—the sensitivity kernels that map these medium perturbations to the splitting intensities (Section 4.5).

4.1 The unperturbed field, Green's functions

The geometrical ray approximation (GRA) to the Green's functions is a causal, short period approximate solution to the elastic wave equation (e.g. Aki & Richards 2002, eq. 2.36), in the frequency domain given by

$$\rho(\mathbf{x})\omega^2 G_{in} + \partial_{x_j}[c_{ijkl}(\mathbf{x})\partial_{x_l} G_{kn}] = -\delta_{in}\delta(\mathbf{x} - \mathbf{x}^s), \quad i, j, k, l, n = 1, 2, 3, \ldots, \tag{11}$$

where ω is angular frequency and $\mathbf{x} = (x_1, x_2, x_3)$ the position vector. Again, the mass density $\rho(\mathbf{x})$ and stiffness tensor $c_{ijkl}(\mathbf{x})$ are smooth functions of $\mathbf{x}$. The right-hand side of eq. (11) represents a point source at $\mathbf{x}^s$ (through the delta function δ) in the canonical directions n

[2]This time reversal appears naturally in the adjoint state formulation. However, the occurrence of both S and u_0 in the right-hand side of (9) illustrates the fundamental difference with reversed time imaging.

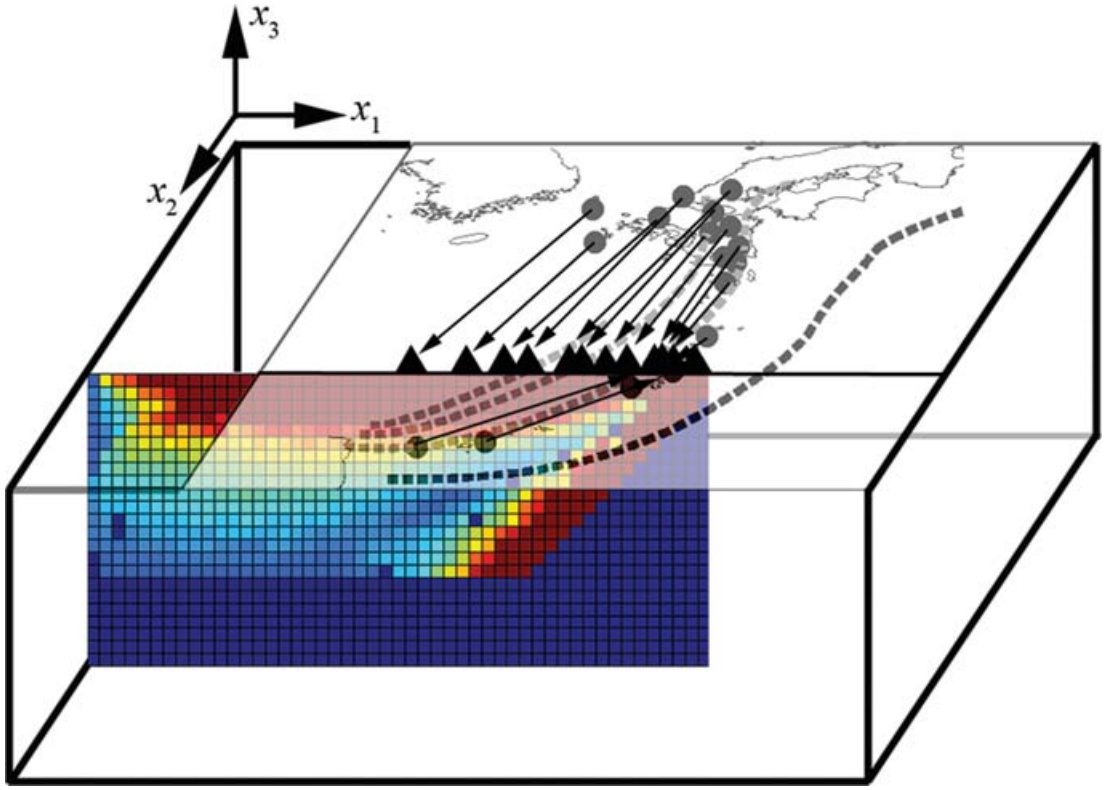

Figure 2. An illustration of the 2.5-D model geometry. As an example, we show the station locations (Long & Van der Hilst 2005, 2006) and starting model for southwestern Japan. Colours represent the strain field from the starting anisotropic model from Long *et al.* (2007). The model is invariant in the x_2 direction. The 2-D station geometry (circles) is then collapsed onto a 1-D line above the starting model.

(through the Kronecker delta, δ_{in}). The Green's function is a sum over the different wave types,[3] where each term is of the form

$$G_{ip}(\mathbf{x}, \omega; \mathbf{x}^s) = A(\mathbf{x}, \mathbf{x}^s) h_i^s(\mathbf{x}) h_p(\mathbf{x}^s) \exp[i\omega T(\mathbf{x}, \mathbf{x}^s)], \tag{12}$$

with $T(\mathbf{x}, \mathbf{x}^s)$the traveltime along the ray segment connecting $\mathbf{x}$ with $\mathbf{x}^s$, and with h_i^s and h_p the components of the (normalized) polarization vectors at the endpoints of the ray. The superscript s indicates explicitly that this polarization vector is associated with the ray originating at the source $\mathbf{x}^s$. With the body force given by (10), subject to replacing $\partial_t H(t)$ by $W^s(t)$, the incident wave is then (asymptotically) represented by

$$u_{0,i}(\mathbf{x}^r, \omega; \mathbf{x}^s) = -W^s(\omega) p_r^s(\mathbf{x}^s) M_{rp}(\mathbf{x}^s) G_{ip}(\mathbf{x}^r, \omega; \mathbf{x}^s). \tag{13}$$

In (12), $A(\mathbf{x}, \mathbf{x}^s)$ is the amplitude, which can be written as (Červený 2001)

$$A(\mathbf{x}, \mathbf{x}^s) = \frac{\exp\left[-i\frac{\pi}{2}\kappa(\mathbf{x}, \mathbf{x}^s)\mathrm{sgn}\omega\right]}{4\pi[\rho(\mathbf{x})v^s(\mathbf{x})\rho(\mathbf{x}^s)v(\mathbf{x}^s)]^{1/2}\,|\det \mathbf{Q}_2(\mathbf{x}, \mathbf{x}^s)|^{1/2}}, \tag{14}$$

where v^s (**x**)and $v(\mathbf{x}^s)$ are the phase velocities at $\mathbf{x}$ and $\mathbf{x}^s$, respectively (evaluated in the direction of the slowness vectors associated with the ray connecting these points) and $|\det \mathbf{Q}_2(\mathbf{x}, \mathbf{x}^s)|^{1/2}$ the relative geometrical spreading given by

$$[Q_2]_{ij}^{-1}(\mathbf{x}, \mathbf{x}^s) = -\frac{\partial^2 T(\mathbf{x}, \mathbf{x}^s)}{\partial q_i^s \partial q_j}, \quad i, j = 1, 2, \tag{15}$$

with q_j and q_i^s local phase-related coordinates in the plane normal to the slowness vectors at $\mathbf{x}^s$ and $\mathbf{x}$, respectively. The KMAH index $\kappa(\mathbf{x},\mathbf{x}^s)$ counts the caustics between $\mathbf{x}^s$ and $\mathbf{x}$; the amplitude A can become complex in the presence of such caustics.

4.2 Projection to the 2-D plane of symmetry

In the 2.5-D approximation the above, general, expressions need to be modified to describe propagation in and out of the 2-D symmetry plane. Here, we choose the second wave front coordinate to coincide with the out-of-plane direction, that is, $q_2 = x_2$, whereas q_1 is in the (x_1, x_3) plane. Then, $\frac{\partial T(\mathbf{x},\mathbf{x}^s)}{\partial q_1^s}$ and $\frac{\partial T(\mathbf{x},\mathbf{x}^s)}{\partial q_1}$ are even functions in x_2, and their derivatives with respect to x_2 vanish: $\frac{\partial^2 T(\mathbf{x},\mathbf{x}^s)}{\partial q_1^s \partial x_2} = \frac{\partial^2 T(\mathbf{x},\mathbf{x}^s)}{\partial x_2^s \partial q_1} = 0$. For this

[3]Unless specifically stated (e.g. in Section 4.3), we do not indicate the mode of propagation in (12) and treat the modes of propagation separately.

choice of coordinates, the geometrical spreading matrix (15) becomes diagonal:

$$\mathbf{Q}_2(\mathbf{x},\mathbf{x}^s)=\begin{bmatrix}\frac{1}{\frac{\partial^2 T(\mathbf{x},\mathbf{x}^s)}{\partial q_1^s \partial q_1}} & 0\\ 0 & \frac{1}{\frac{\partial p_2}{\partial x_2}}\end{bmatrix}=\begin{bmatrix}Q_2^{\|}(\mathbf{x},\mathbf{x}^s) & 0\\ 0 & Q_2^{\perp}(\mathbf{x},\mathbf{x}^s)\end{bmatrix}, \tag{16}$$

with $Q_2^{\|}(\mathbf{x},\mathbf{x}^s)$ and $Q_2^{\perp}(\mathbf{x},\mathbf{x}^s)$ the in- and out-of-plane relative geometrical spreading factors, respectively. Thus the geometrical spreading factors into an in- and an out-of-plane component, that is, $|\det\mathbf{Q}_2(\mathbf{x},\mathbf{x}^s)| = |Q_2^{\|}(\mathbf{x},\mathbf{x}^s)Q_2^{\perp}(\mathbf{x},\mathbf{x}^s)|^{1/2}$. The in-plane amplitude can then be expressed as

$$A^{\|}(\mathbf{x},\mathbf{x}^s)=\frac{\exp\left[-i\frac{\pi}{2}\kappa(\mathbf{x},\mathbf{x}^s)\mathrm{sgn}\omega\right]}{4\pi[\rho(\mathbf{x})v^s(\mathbf{x})\rho(\mathbf{x}^s)v(\mathbf{x}^s)]^{1/2}|Q_2^{\|}(\mathbf{x},\mathbf{x}^s)|^{1/2}}. \tag{17}$$

4.3 The perturbed field and the (high-frequency) Born approximation

We derive the 2.5-D Born modelling formula using a stationary phase argument and integrating over x_2, the out-of-plane coordinate (Foss *et al*. 2005). From now on, the position vector $\mathbf{x}=(x_1,x_3)$. The stationary phase argument involves the condition

$$\partial_{x_2}[T(\mathbf{x}^s,\mathbf{x})+T(\mathbf{x},\mathbf{x}^r)]=p_2^s+p_2^r=0, \tag{18}$$

where p_2^s and p_2^r are components of the slowness vectors p^s and p^r associated with the source and the receiver rays. For our inversion problem (see also Section 5.1) we consider in-plane scattering only, so that $p_2^s=p_2^r=0$. In accordance with our earlier notation, we have $h^s=h_0$; likewise, we write $T=T_0$, $p^s=p_0$, $A^{\|}=A_0^{\|}$ and $Q_2^{\perp}=Q_{2;0}^{\perp}$, with the understanding that, in the following analysis, the subscript $_0$ will always be identified with (q)SV propagation. The (q)SV polarization is extracted through contracting $u_{0,i}(\mathbf{x}^r,\omega,\mathbf{x}^s)$ with ${}^Rh_{0,i}(\mathbf{x}^r)$, as before, and substituting ${}^Rh_{0,p}(\mathbf{x}^s)$ for $h_p(\mathbf{x}^s)$ in (12).

For the description of the perturbed wavefield in the (anisotropic) region under study we need to consider mode conversions from (q)SV (that is, the background field u_0) to (q)SH. With u_{mn} denoting the m-component of the perturbed wavefield due to a body force in direction n and with α and β indicating the propagation modes, that is, $\alpha=$ (q)SV and $\beta=$ (q)SV, (q)SH, we use the results derived in the sections above to obtain[4]:

$$u_{mn}^{\beta\alpha}(\mathbf{x}^r,t;\mathbf{x}^s)\approx\sqrt{\frac{\mathrm{i}}{2\pi}}\int\int_{\mathbb{R}}{}^{\beta}h_m^r(\mathbf{x}^r)\omega^{3/2}\rho(\mathbf{x})\frac{A_\alpha^{\|}(\mathbf{x}^s,\mathbf{x})A_\beta^{\|}(\mathbf{x},\mathbf{x}^r)}{\mathcal{L}_{\beta\alpha}^{\perp}(\mathbf{x}^r,\mathbf{x},\mathbf{x}^s)}\,\mathbf{w}_{\beta\alpha}^T(\mathbf{x}^r,\mathbf{x},\mathbf{x}^s)\delta\mathbf{c}(\mathbf{x})\exp\left[\mathrm{i}\omega T_{\beta\alpha}(\mathbf{x}^r,\mathbf{x},\mathbf{x}^s)-t\right]{}^{\alpha}h_n^s(\mathbf{x}^s)d\omega d\mathbf{x}. \tag{19}$$

Using (13) gives for the m-component of the perturbed wavefield

$$\begin{aligned}\delta u_m^{\beta\alpha}(\mathbf{x}^r,t;\mathbf{x}^s)\approx&-\sqrt{\tfrac{\mathrm{i}}{2\pi}}\int\int_{\mathbb{R}}{}^{\beta}h_m^r(\mathbf{x}^r)\omega^{3/2}\rho(\mathbf{x})\frac{A_\alpha^{\|}(\mathbf{x}^s,\mathbf{x})A_\beta^{\|}(\mathbf{x},\mathbf{x}^r)}{\mathcal{L}_{\beta\alpha}^{\perp}(\mathbf{x}^r,\mathbf{x},\mathbf{x}^s)}\,\mathbf{w}_{\beta\alpha}^T(\mathbf{x}^r,\mathbf{x},\mathbf{x}^s)\delta\mathbf{c}(\mathbf{x})\exp\left[\mathrm{i}\omega T_{\beta\alpha}(\mathbf{x}^r,\mathbf{x},\mathbf{x}^s)-t)\right]^{\alpha}\\&\times p_r^s(\mathbf{x}^s)M_{rn}(\mathbf{x}^s)^{\alpha}h_n^s(\mathbf{x}^s)W^s(\omega)\,d\omega d\mathbf{x}.\end{aligned} \tag{20}$$

Here, the refracted traveltime is given by

$$T_{\beta\alpha}(\mathbf{x}^r,\mathbf{x},\mathbf{x}^s)=T_\alpha(\mathbf{x}^s,\mathbf{x})+T_\beta(\mathbf{x},\mathbf{x}^r), \tag{21}$$

the refracted out-of-plane geometrical spreading by

$$\mathcal{L}_{\beta\alpha}^{\perp}(\mathbf{x}^r,\mathbf{x},\mathbf{x}^s)=\left|Q_{\alpha;2}^{\perp}(\mathbf{x}^s,\mathbf{x})+Q_{\beta;2}^{\perp}(\mathbf{x},\mathbf{x}^r)\right|^{1/2}, \tag{22}$$

and the associated radiation patterns (e.g. Ben-Menahem *et al.* 1991) by $\mathbf{w}_{\beta\alpha}(\mathbf{x}^r,\mathbf{x},\mathbf{x}^s)$. We can now write the expression for the transverse component of the perturbed wavefield as a function of the medium perturbations δc. In our application,

$$\begin{aligned}\delta u(\mathbf{x}^r,t;\mathbf{x}^s)^T\approx&-{}^Th_{0,m}(\mathbf{x}^r)\sum_{\beta=(\mathrm{q})\mathrm{SV},(\mathrm{q})\mathrm{SH}}\sqrt{\frac{\mathrm{i}}{2\pi}}\int\int_{\mathbb{R}}{}^{\beta}h_m^r(\mathbf{x}^r)\omega^{3/2}\rho(\mathbf{x})\frac{A_\alpha^{\|}(\mathbf{x}^s,\mathbf{x})A_\beta^{\|}(\mathbf{x},\mathbf{x}^r)}{\mathcal{L}_{\beta\alpha}^{\perp}(\mathbf{x}^r,\mathbf{x},\mathbf{x}^s)}\,\mathbf{w}_{\beta\alpha}^T(\mathbf{x}^r,\mathbf{x},\mathbf{x}^s)\delta\mathbf{c}(\mathbf{x})\\&\cdot\exp\left[i\omega\left(T_{\beta\alpha}(\mathbf{x}^r,\mathbf{x},\mathbf{x}^s)-t\right)\right]^{\alpha}p_r^s(\mathbf{x}^s)M_{rn}(\mathbf{x}^s)^{\alpha}h_n^s(\mathbf{x}^s)W^s(\omega)d\omega\,\mathrm{d}\mathbf{x},\ \alpha=(\mathrm{q})\mathrm{SV}.\end{aligned} \tag{23}$$

Note than in (23) we sum over the (q)SV and (q)SH components of the perturbed wavefield. In the 2.5-D approximation, with ${}^{\alpha}p_2^s={}^{\beta}p^r{}_2=0$, the polarizations of qP and qSV waves satisfy $h_2=0$ whereas the polarization of qSH is given by (0, 1, 0).

[4]The refracted traveltime given can be multivalued in the presence of caustics. In that case, we must replace (19) by the sum over the different traveltime branches. This is assumed implicitly in the text.

4.4 Medium perturbations and radiation patterns

With invariance in the x_2 direction and $(x_1, x_3)$the symmetry plane, the stiffness tensor can be written in the form:

$$\{c_{ijkl}\} \rightarrow c_{ij} = \begin{bmatrix} c_{1111} & c_{1122} & c_{1133} & 0 & 2c_{1113} & 0 \\ c_{1122} & c_{2222} & c_{2233} & 0 & 2c_{2213} & 0 \\ c_{1133} & c_{2233} & c_{3333} & 0 & 2c_{3313} & 0 \\ 0 & 0 & 0 & 4c_{2323} & 0 & 4c_{2312} \\ 2c_{1113} & 2c_{2213} & 2c_{3313} & 0 & 4c_{1313} & 0 \\ 0 & 0 & 0 & 4c_{2312} & 0 & 4c_{1212} \end{bmatrix}. \tag{24}$$

This representation allows for transversely isotropic (TI) media that is tilted in the (x_1, x_3)-plane, as well as TI media with symmetry axes aligned with the x_2-axis. In this coordinate system, the stiffness tensor has 13 independent elements; with higher symmetry, such as isotropy, this number reduces accordingly. The medium perturbations are collected in the (13-element) model vector (see also Chapman & Pratt 1992):

$$\delta\mathbf{c}(\mathbf{x}) = \left\{ \frac{\delta c_{ijkl}(\mathbf{x})}{\rho(\mathbf{x})} \right\}. \tag{25}$$

Following Burridge *et al.* (1998), the corresponding radiation patterns are

$$\mathbf{w}_{\beta\alpha}(\mathbf{x}^r, \mathbf{x}, \mathbf{x}^s) = \left\{ {}^{\alpha}h_i^s(\mathbf{x}) {}^{\alpha}p_j^s(\mathbf{x}) {}^{\beta}h_k^r(\mathbf{x}) {}^{\beta}p_l^r(\mathbf{x}) \right\}, \tag{26}$$

where the indices follow those of the stiffness matrix in the ordering defined by the matrix or inner product $\mathbf{w}_{\beta\alpha}^T(\mathbf{x}^r, \mathbf{x}, \mathbf{x}^s)\delta\mathbf{c}(\mathbf{x})$ in (19). For our 2.5-D problem, the out-of-plane slownesses are zero (${}^{\alpha}p_2^s = {}^{\beta}p_2^r = 0$) and the contributions to (26) vanish for $j, l = 2$ in c_{ijkl}. This reduces the number of independent elastic parameters from 13 to 7.

4.5 The sensitivity kernel

We now return to the expression we have obtained for the perturbed wavefield (eq. 19) and the relationship between the perturbed elastic constants and the splitting intensity observed at the surface (eq. 5). In Section 3, we obtained a forward modelling operator F (that is, the normalization of operator H) that, according to (6), acts on $\delta\mathbf{c}$ to produce the splitting intensity observations S. From this relationship we can derive an expression for the sensitivity kernel using a series of simplifications based on the geometries of the rays in our splitting data set and on the 2.5-D geometry of our problem. Substituting the wavefield expression (19) into (4) yields

$$\begin{aligned} H\delta\mathbf{c}(\mathbf{x}^s, \mathbf{x}^r) &= -\int \overline{u_0(\mathbf{x}^r, \omega; \mathbf{x}^s)^R} \mathrm{i}\omega [\delta u(\mathbf{x}^r, \omega; \mathbf{x}^s)]^T d\omega \\ &= \int \Bigg\{ \sum_{\beta=(\mathrm{q})\mathrm{SV},(\mathrm{q})\mathrm{SH}} -\sqrt{\frac{\mathrm{i}}{2\pi}} \int_{\mathbb{R}} {}^T h_{0,m}(\mathbf{x}^r) {}^{\beta}h_m^r(\mathbf{x}^r) \mathrm{i}\omega^{5/2} \rho(\mathbf{x}) \frac{A_{\alpha}^{||}(\mathbf{x}^s, \mathbf{x}) A_{\beta}^{||}(\mathbf{x}, \mathbf{x}^r)}{L_{\beta\alpha}^{\perp}(\mathbf{x}^r, \mathbf{x}, \mathbf{x}^s)} \frac{\overline{A_0^{||}(\mathbf{x}^r, \mathbf{x}^s)}}{\left|Q_{0;2}^{\perp}(\mathbf{x}^r, \mathbf{x}^s)\right|^{1/2}} \\ &\quad \times M_{rp}(\mathbf{x}^s) p_{0,r}(\mathbf{x}^s) h_{0,p}(\mathbf{x}^s) M_{r'p'}(\mathbf{x}^s) {}^{\alpha}p_{r'}^s(\mathbf{x}^s) {}^{\alpha}h_{p'}^s(\mathbf{x}^s) \\ &\quad \times \exp\left[i\omega (T_{\beta\alpha}(\mathbf{x}^r, \mathbf{x}, \mathbf{x}^s) - T_0(\mathbf{x}^r, \mathbf{x}^s)) \right] |W^s(\omega)|^2 \, d\omega \mathbf{w}_{\beta\alpha}^T(\mathbf{x}^r, \mathbf{x}, \mathbf{x}^s) \Bigg\} \delta\mathbf{c}(\mathbf{x}) d\mathbf{x}. \end{aligned} \tag{27}$$

In the 2.5-D approximation, the energy normalization factor, defined below eq. (5), becomes

$$\tilde{N}_{s,r} \simeq \frac{\left|A_0^{||}(\mathbf{x}^r, \mathbf{x}^s)\right|^2}{\left|Q_{0;2}^{\perp}(\mathbf{x}^r, \mathbf{x}^s)\right|^2} [M_{rp}(\mathbf{x}^s) h_{0;p}(\mathbf{x}^s) p_{0;r}(\mathbf{x}^s)]^2 \int \omega^2 |W^s(\omega)|^2 \, \mathrm{d}\omega. \tag{28}$$

With the expression between braces in (27), and the expression for the normalization factor in (28), we have the components to generate the form of the sensitivity kernels in (3). We proceed by using some physical insights.

Since the source is far away from the mantle region where we aim to constrain $\delta\mathbf{c}$ we can make several simplifications. First, because the difference in propagation direction of the perturbed and unperturbed rays (far from the source, see Fig. 1) is small we can write

$${}^{\alpha}p_r^s(\mathbf{x}^s) \simeq p_{0,r}(\mathbf{x}^s) {}^{\alpha}h_p^s(\mathbf{x}^s) \simeq h_{0,p}(\mathbf{x}^s). \tag{29}$$

Furthermore, since the distance from the source position to $\mathbf{x}$ in the target region is much larger than the distance from $\mathbf{x}$ to the receiver, the expressions for the geometrical spreading factors obtained in Section 4.2 can be simplified:

$$\frac{1}{\left|Q_{\alpha;2}^{||}(\mathbf{x}^s, \mathbf{x})\right|^{1/2} Q_{\beta;2}^{||}(\mathbf{x}, \mathbf{x}^r)\right|^{1/2}} \simeq \frac{1}{\left|Q_{\beta;2}^{||}(\mathbf{x}^r, \mathbf{x})\right|^{1/2}} \frac{1}{\left|Q_{0;2}^{||}(\mathbf{x}^r, \mathbf{x}^s)\right|^{1/2}}, \tag{30}$$

and

$$\frac{1}{\left|Q_{\alpha;2}^{\perp}(\mathbf{x}^s, \mathbf{x}) + Q_{\beta;2}^{\perp}(\mathbf{x}, \mathbf{x}^r)\right|^{1/2}} \simeq \frac{1}{\left|Q_{\alpha;2}^{\perp}(\mathbf{x}^s, \mathbf{x})\right|^{1/2}} \simeq \frac{1}{\left|Q_{0;2}^{\perp}(\mathbf{x}^r, \mathbf{x}^s)\right|^{1/2}}. \tag{31}$$

As a consequence,

$$\frac{A^{\|}_{\alpha}(\mathbf{x}^s,\mathbf{x})A^{\|}_{\beta}(\mathbf{x},\mathbf{x}^r)}{\mathcal{L}^{\perp}_{\beta\alpha}(\mathbf{x}^r,\mathbf{x},\mathbf{x}^s)} \simeq A^{\|}_{\beta}(\mathbf{x}^r,\mathbf{x})\frac{[\rho(\mathbf{x}^r)^{\alpha}v^s(\mathbf{x}^r)]^{1/2}}{[\rho(\mathbf{x})^{\alpha}v^s(\mathbf{x})]^{1/2}}\frac{A^{\|}_{0}(\mathbf{x}^r,\mathbf{x}^s)}{\left|\mathcal{Q}^{\perp}_{0;2}(\mathbf{x}^r,\mathbf{x}^s)\right|^{1/2}}. \tag{32}$$

With these approximations, the sensitivity kernel $\mathcal{K}$, which relates linearly the medium perturbations $\delta\mathbf{c}$ to splitting intensities, can be obtained from (27) and (28):

$$\begin{aligned}\mathcal{K}(\mathbf{x}^s,\mathbf{x}^r;\mathbf{x}) \simeq &\left[\int \omega^2\,|W^s(\omega)|^2\,d\omega\right]^{-1}\sum_{\beta=(\mathrm{q})\mathrm{SV},(\mathrm{q})\mathrm{SH}} {}^{T}h_{0,m}(\mathbf{x}^r)^{\beta}h^r_m(\mathbf{x}^r)\\ &\times(-)\sqrt{\frac{\mathrm{i}}{2\pi}}\int \mathrm{i}\omega^{5/2}\rho(\mathbf{x})\frac{[\rho(\mathbf{x}^r)^{\alpha}v^s(\mathbf{x}^r)]^{1/2}}{[\rho(\mathbf{x})^{\alpha}v^s(\mathbf{x})]^{1/2}}A^{\|}_{\beta}(\mathbf{x}^r,\mathbf{x})\\ &\times\exp\left[i\omega(T_{\beta\alpha}(\mathbf{x}^r,\mathbf{x},\mathbf{x}^s)-T_0(\mathbf{x}^r,\mathbf{x}^s)\right]|W^s(\omega)|^2\,d\omega\mathbf{w}^T_{\beta\alpha}(\mathbf{x}^r,\mathbf{x},\mathbf{x}^s),\ \alpha=(\mathrm{q})\mathrm{SV}.\end{aligned} \tag{33}$$

In Appendix B, we compare this form of the sensitivity kernel to the 2-D kernel formulation in Favier & Chevrot (2003). In Section 5, we describe the anisotropy in the 2-D plane by means of two parameters (dip and strength); to obtain the associated kernels we express each term in the perturbed elastic tensor $\delta\mathbf{c}$ in terms of these two parameters (see also Appendix C). In Section 5, we also discuss some computational aspects and give examples of kernels for several different types of background medium. The implementation of such kernels in tomography is briefly discussed in Section 6.

5 COMPUTATION AND EXAMPLES OF SENSITIVITY KERNELS FOR 2-D SUBDUCTION MODELS

We illustrate the general concepts and theory described above with several examples of splitting intensity kernels in the context of our study of upper-mantle anisotropy beneath southwestern Japan with splitting intensity functions from *SKS*, *SKKS* and teleseismic *S* data (Long & Van der Hilst 2005a, 2006). For illustration purposes, we consider three stations of the Japanese F-net array (www.fnet.bosai.go.jp).

5.1 SHEAR WAVE SPLITTING DATA CONSISTENT WITH 2.5-D APPROXIMATION

From a structure point of view, the invariance along the strike of simple subduction zones justifies the use of a 2-D plane of symmetry. Do the data also satisfy the conditions justifying the 2.5-D approximation? After all, we use the 2.5-D Born approximation to derive in-plane scattering coefficients (see Section 4.2) and departures of the ray path from the symmetry plane will cause these coefficients to be inaccurate. For our data set we expect the error to be small, because the waves from which splitting functions are used propagate in or near the chosen 2-D plane.

Incidence angles of *SKS* and *SKKS* waves are small, and irrespective of backazimuth the propagation direction is within $\sim 10^{\circ}$ (SKS) or $15–20^{\circ}$ (SKKS) of the 2-D symmetry plane beneath the study area. Teleseismic *S* waves have a larger horizontal slowness and will have a substantial out-of-plane component if they arrive from backazimuths that do not coincide with the strike of the symmetry plane. Fortunately, most of the direct teleseismic *S* waves considered by Long & Van der Hilst (2005a) originate in the southwestern Pacific and arrive parallel to the 2-D plane used. Direct *S* from backazimuths not along the symmetry plane will not be used in the tomographic inversions with the 2.5-D approach presented here.

5.2 ANISOTROPIC BACKGROUND MODELS FOR THE KERNEL CALCULATION

For the calculation of the Green's functions and, thus, the sensitivity kernels in the previous section we use 2-D heterogeneous, anisotropic background models[5] based on calculations of upper-mantle flow (Long *et al.* 2007). The details of those calculations are not important for the illustration of the kernels associated with the type of anisotropic medium thus produced, but we summarize here the most relevant aspects.

The objective of Long *et al.* (2007) was to produce 2-D anisotropic models that are consistent with the observed splitting data and that provide a suitable starting point for tomographic inversion. Constructing and selecting such models involves several steps. First, for a range of different rheologies and with (or without) localized occurrence of so-called B-type fabric (where the fast axis of anisotropy is oriented 90° from the plane of the flow model, that is, in the x_2–x_3 plane), numerical (finite element) modelling is used to constrain flow patterns in the mantle wedge above a kinematically defined subducting plate. Second, after obtaining steady-state, streamlines are traced through the velocity field and the evolution of finite strain along them is calculated with the approach of McKenzie (1979). Third, the orientation of the finite strain

[5]There is a distinction between the isotropic background medium referred to in Section 3 (which results in the 'unperturbed' field u_0) and the reference model used in the kernel computations in this section. In the sense that the 'background medium' represents the unperturbed wavefield—that is, without the effect of anisotropy—we do use an isotropic background medium to derive our sensitivity kernels. Additionally, we do the ray tracing described in this section in an isotropic background model (ak135). However, the reference model used to calculate the perturbation in elastic parameters—that is, the derivatives in eq. (35)—is anisotropic.

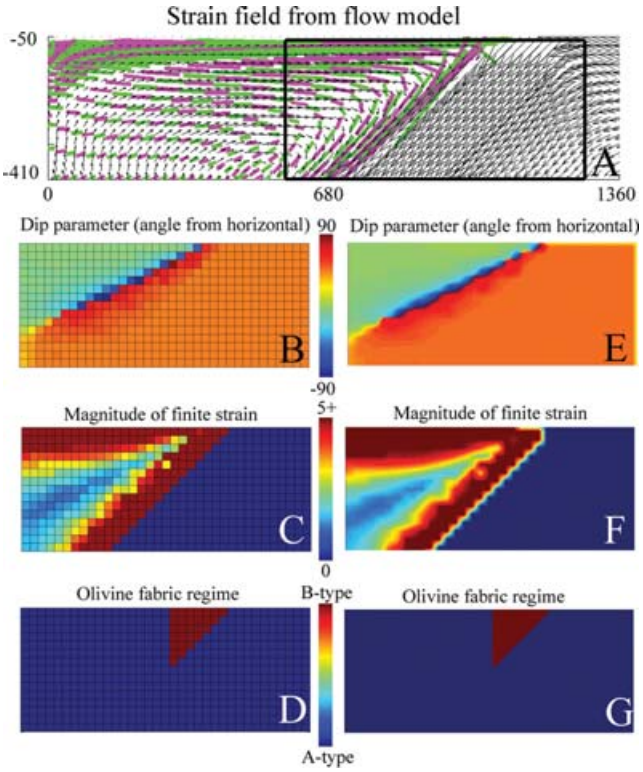

Figure 3. (a) Distribution of finite strain ellipses in the mantle wedge for Model A from Long *et al.* (2007), the background model used for heterogeneous kernel computations. The vertical and horizontal coordinates are given in kilometres. The black box outlines the area of the flow model that is considered in the kernel computation. (b) Distribution of the dip parameter θ_0 in the starting model for the region corresponding to the black box in (a). (c) Magnitude of the maximum finite strain (stretch ratio) in the starting model. The colour scale saturates at a stretch ratio of 5. (d) Distribution of A- and B-type olivine fabric in the starting model. The B-type fabric regime is shown in red. We note that for illustration purposes, we have exaggerated the size of the B-type region somewhat—a region this large is not required to fit the splitting data (Long *et al.* 2007). (e–g) Interpolated version of the coarse grid starting model shown in panels (b–d). We use the finer grid version of the background model in the kernel computation.

ellipse is used as a proxy for the geometry of anisotropy (that is, the orientation of the fast axis). Fourth, anisotropy in the 2-D plane is defined by elastic constants similar to those for tilted transverse isotropy (TTI): θ_0 measures the dip of the ellipse with respect to horizontal and ε_A represents the strength of anisotropy (see Section 5.3). Finally, from the anisotropic models synthetic splitting data are calculated with ray perturbation theory for a TTI medium (Chevrot & Van der Hilst 2003) and tested against the observations. Long *et al*. (2007) thus found that B-type olivine fabric (up to ∼100–125 km from the trench) is needed to match the observed trench-parallel fast directions near the trench (Long & Van der Hilst 2006).

In later sections we illustrate kernel properties using two types of background: a single, homogenous layer of anisotropy and a heterogeneous (subduction zone) model. As an example of the latter, Fig. 3 depicts the distributions of finite strain, dip (θ_0), anellipticity (ε_A) and B-type fabric for one of the mantle wedge models produced by Long *et al.* (2007). For illustration purposes, we exaggerate the size of the B-type region.

5.3 Parametrization of anisotropy in the 2-D symmetry plane

Anisotropy in the upper mantle is generally interpreted in terms of lattice preferred orientation of olivine; olivine is orthorhombic but experimental and petrographic studies have shown that deformed polycrystalline olivine aggregates generally have nearly hexagonal (TI) symmetry (Zhang & Karato 1995; Ismail & Mainprice 1998). Subsequent studies (e.g. Browaeys & Chevrot 2004; Becker *et al.* 2006) have demonstrated that the strength of upper-mantle anisotropy can be generally well represented by a single parameter. Based on these mineral physics considerations, and based on our experience with 2-D modelling of subduction zones and our success in matching the broad features of the F-net data set with corner flow type models (Long *et al*. 2007), we represent anisotropy in our models with three parameters, representing the direction (azimuth and dip) and the strength of anisotropy.

The azimuth describes the orientation of the long axis of the strain ellipse in the horizontal plane. With the 2.5-D approximation it cannot be resolved and is taken from the starting models. The dip parameter θ_0 denotes the angle between the strain ellipse and the horizontal plane. The anellipticity parameter ε_A measures the strength of anisotropy and can be written as a combination of elements of the elastic tensor:

$$\varepsilon_A \equiv \frac{(c_{11}-c_{55})(c_{33}-c_{55})-(c_{13}+c_{55})^2}{(c_{11}-c_{55})(c_{33}-c_{55})}. \tag{34}$$

The anellipticity is a convenient parameter to work with, under the assumption that anisotropy in the upper mantle can be represented by three parameters, one of which describes the strength of anisotropy. For transverse isotropic media ε_{A} is always greater than zero (e.g. Schoenberg & De Hoop 2000); we assume that it increases linearly with strain until saturation occurs near $\gamma \approx 2-3$ (e.g. Zhang & Karato 1995). This increase in ε_{A} with strain, to a maximum value, mimics the saturation of the LPO texture. [For the model used in Section 5.5 we have a maximum value $\varepsilon_{\mathrm{A_{MAX}}} = 0.15$, which corresponds to the transversely isotropic mantle (TIM) model of Chevrot & van der Hilst (2003).] Although our simplified parametrization may not completely capture the complexity of 3-D variations of anisotropy in the upper mantle, it makes use of reasonable prior assumptions about LPO development that can simplify the inversion framework. Of course, other parametrizations (e.g. Becker *et al*. 2006) are possible and easy to implement since we have not, until now, made any assumptions about the parametrization scheme.

With the azimuth fixed, the inversion scheme solves, for each model block, only two independent anisotropic parameters: θ_0 and ε_{A}. To derive sensitivity kernels for θ_0 and ε_{A}—instead of medium perturbation $\delta\mathbf{c}$, as in (33)—we must express each term in the perturbed elastic tensor $\delta\mathbf{c}$ in terms of these parameters. The definition, rotation, and perturbation of the stiffness tensor are given in Appendix C. The total perturbation in the stiffness tensor component can be written as (Appendix C, eq. C14):

$$\delta\mathbf{c} = \delta c_{\varepsilon_A} + \delta c_\theta = \frac{\partial \mathbf{c}}{\partial \varepsilon_A}\delta\varepsilon_A + \frac{\partial \mathbf{c}}{\partial \theta_0}\delta\theta_0. \tag{35}$$

Because ε_{A} increases linearly with increasing strength of anisotropy, the derivatives with respect to it are computed over a range of values, from isotropy to transverse isotropy.

The fact that azimuth is fixed also implies that if B-type fabric occurs we, in fact, compute two separate kernels: one for fast polarization axes in the x_1–x_3 plane (azimuth $= 90^\circ$) and, in mantle regions with B-type fabric, one for fast axes in the x_2–x_3 plane (azimuth $= 0^\circ$).

5.4 Ray geometry and frequency spectrum

Using (33) and (35) we compute the contribution to the sensitivity kernel K for θ_0 and ϵ_{A} at each scattering point $\mathbf{x}$ in the study region. A schematic diagram of the kernel calculation is shown in Fig. 1(b). For each $\mathbf{x}$ we calculate the slowness vectors $\mathbf{p}$ and the unit polarization vectors $\mathbf{h}$ for two segments of the broken ray: $\boldsymbol{x}^{\mathbf{s}} \longrightarrow \boldsymbol{x}$ and $\boldsymbol{x} \longrightarrow \boldsymbol{x}^{\mathbf{r}}$; the vectors $\mathbf{p}^r$, $\mathbf{p}^s$, $\mathbf{h}^r$ and $\mathbf{h}^s$ form the radiation pattern vector $\mathbf{w}$ according to (26). The in-plane geometrical spreading is calculated between $\mathbf{x}$ and $\mathbf{x}^r$ (30, 31). The isotropic background shear velocities $v(\mathbf{x})$ and associated mass densities $\rho(\mathbf{x})$ are based on *ak*135 (Kennett *et al*. 1995; Montagner & Kennett 1995). The traveltime difference between the unperturbed and perturbed rays, that is, $T(\mathbf{x}^r, \mathbf{x}, \mathbf{x}^s) - T_0(\mathbf{x}^r, \mathbf{x}^s)$, is calculated with respect to *ak*135; slowness vectors, traveltime differences, and amplitudes $A^{||}(\mathbf{x}^r,\mathbf{x})$ are calculated by 2-D ray tracing.

The frequency spectrum of the incident shear wave is

$$|W^s(\omega)|^2 = \frac{\omega^2\tau^2}{4\pi}e^{-\omega^2\tau^2/8\pi^2}, \tag{36}$$

where τ is the characteristic period of the wave. Following the approach of Favier & Chevrot (2003), we approximate the spectrum as the second derivative of a Gaussian; this is reasonable for *SKS*-type phases where the records have been deconvolved from the radial component waveform (Chevrot 2000; Long & Van der Hilst 2005a). We use a characteristic period of $\tau = 8$ s for direct *S* phases, $\tau = 10$ s for *SK*(*K*)*S* phases. The integrals over frequency in eq. (33) are computed using the trapezoidal rule over the same frequency range (0.02–0.125 Hz) as used by Long & Van der Hilst (2005a).

Finally, at each scattering point $\mathbf{x}$ we compute the partial derivatives of $\delta\mathbf{c}$ with respect to the anisotropic parameters θ_0 and ε_{A} in order to obtain sensitivity kernels $\mathcal{K}(\theta_0)$ and $\mathcal{K}(\varepsilon_{\mathrm{A}})$ (Section 5.3; Appendix C).

5.5 Kernel examples; the importance of the background medium

In Figs 4–6 we show examples of sensitivity kernels $\mathcal{K}(\theta_0)$ and $\mathcal{K}(\epsilon_{\mathrm{A}})$ calculated for shear arrivals in our splitting data set. In Fig. 4 we show a series of kernels for a homogenous background (with θ_0 zero everywhere), calculated on a fine grid ($\sim$4 km spacing), for four different ray paths: a direct *S* arrival at station FUK, an *SKS* arrival at station YTY and two direct *S* arrivals from opposite backazimuths at station TKA. The kernels display familiar oscillatory behaviour (e.g. Hung *et al.* 2000; Chevrot *et al.* 2004; De Hoop & Van der Hilst 2005a). These results are similar to the 2-D sensitivity kernels in Favier & Chevrot (2003), except that we allow for non-vertical incidence.

Figs 5 and 6 displays kernel for the same ray paths, but now they are calculated with respect to the heterogeneous, anisotropic models depicted in Figs 3(b)–(d). In Fig. 5, we show one kernel example for the same arrival shown in Fig. 4(a), for a heterogeneous background model similar to that shown in Fig. 3, but without the B-type region in the mantle wedge. In Fig. 6, we show kernels for the same four ray paths shown in Fig. 4, for our preferred model which includes a B-type region. For this computation, we perturb the anisotropic parameters at each point in the starting model and compute (numerically) the derivatives in eq.(35). The local values of the partial derivatives $\frac{\partial c}{\partial \varepsilon_A}$ and $\frac{\partial c}{\partial \theta_0}$, and, therefore, the local sensitivity to the anisotropic parameters, depend strongly on the starting model. Consequently, the use of a heterogeneous background

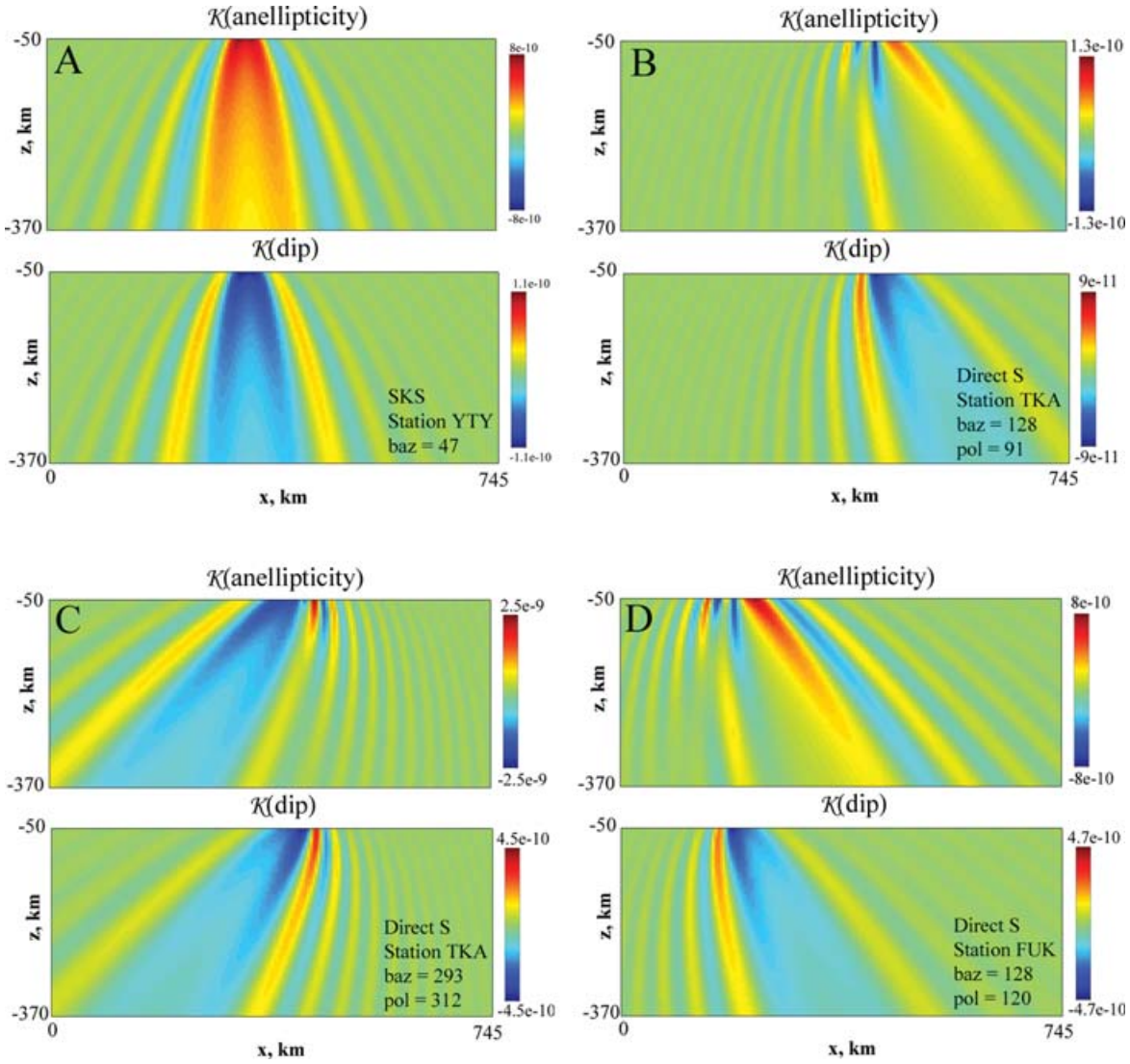

Figure 4. (a–d) Examples of sensitivity kernels for parameters ϵ_A (top) and θ_0 (bottom) for four shear arrivals in the splitting data set. (a) An *SKS* phase (backazimuth = 47°) recorded at station YTY. (b) A direct *S* phase from an event in Tonga (backazimuth = 128°, incoming polarization direction = 91°) recorded at station TKA. (c) A direct *S* phase from an event in the Hindu Kush region (backazimuth = 293°, incoming polarization direction = 312°) recorded at station TKA. (d) A direct *S* phase from an event in Tonga (backazimuth = 128°, incoming polarization direction 120°) recorded at station FUK. All sensitivities are given in s m^{-2} and are calculated with respect to a homogenous anisotropic model with a horizontal symmetry axis.

medium leaves a strong 'imprint' on the kernels; locally the sensitivity can even be opposite of that for a homogeneous background. Indeed, the differences between the kernels shown in Figs 4–6 demonstrate the profound effect of the (heterogeneous) background model (see also De Hoop & Van der Hilst 2005a, b, 2006). This is true for models both without (Fig. 5) and with (Fig. 6) the B-type region that is included in the preferred model of Long *et al.* (2007).

The superposition of sensitivity kernels for multiple arrivals in the southwestern Japan data set begins to reveal the localization of signal from distinct anisotropic regions (Fig. 7). We stress, again, that the spatial resolution implied in the localization shown in Fig. 7 will only be meaningful, and the inversion result accurate, if the kernels are properly (that is, iteratively) calculated in a reference model that has the same type of heterogeneity as in the medium under investigation. Indeed, the use of finite frequency kernels computed in a homogeneous background may well give a false perception of improved resolution. Calculating such kernels for all the data enables the construction of the normal equations to carry out the tomographic inversion.

Fig. 6 demonstrates the localization properties of such kernels due to the presence of a mantle wedge region with B-type fabric. However, the sharp transitions in the kernel between the B-type fabric region in the wedge corner and normal fabric elsewhere also suggest that the incorrect assessment of the location and spatial extent of such a wedge can result in significant imaging artefacts. One strategy for dealing with this ambiguity involves trying starting models with different-sized and -shaped B-type regions and assessing the differences in the resulting tomographic images. However, another, perhaps more promising strategy would be to incorporate the boundary of the B-type region as free

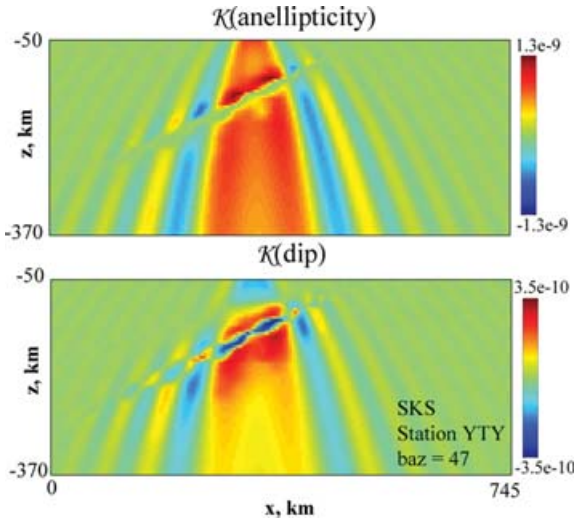

Figure 5. An example of a sensitivity kernel computed in a heterogeneous, anisotropic background model. The kernel is computed for the same event as in Fig. 4(a). For a starting model, we use the model shown in Fig. 3, but without the region of B-type fabric. All sensitivities are given in s m^{-2}. For the kernel computation, the starting model, calculated on the coarse grid (21.25 × 21.25 km) used in the flow modelling framework (see Long *et al.* 2007), is interpolated (cubic interpolation) to a finer grid spacing (∼4 km).

parameters in the inversion. This involves the use of a 'shape optimization' formulation, which can also be used in the imaging of, for instance, the (unknown) flanks of salt bodies.

6 DISCUSSION

We have presented the theory needed to compute sensitivity kernels for wave equation shear wave splitting intensity tomography of upper-mantle anisotropy in backarc mantle wedges. The details of the tomographic inversion of data from southwestern Japan will be presented elsewhere (Long *et al.* in preparation).

Tomographic inversions of splitting data are highly non-linear. Chevrot (2006) proposes the use of an iterative Gauss–Newton algorithm to address this challenge. We deal with the non-linearity by computing kernels in heterogeneous, anisotropic reference models that already come close to matching the observed splitting and by iterating between updates to the tomographic model and updates to the flow modelling parameters. In this scheme, the constraints from the solution of equations that govern viscous flow in the mantle wedge inform our choice of starting model for the inversion and, vice versa, the inversion constraints on anisotropic structure are used to update the flow models.

The work presented here builds on previous work in wave equation tomography for transmitted (De Hoop & Van der Hilst 2005a) and reflected (De Hoop *et al.* 2006) phases, as well as on previous work on finite-frequency sensitivity kernels for shear wave splitting (Favier & Chevrot 2003; Chevrot *et al.* 2004; Chevrot 2006). We make several new contributions. First, we derive the full PDE formulation that governs wave equation splitting tomography and show that the PDEs are similar in structure to those governing wave equation transmission and reflection tomography. This paves the way for the joint tomographic inversion of types of data with different sensitivities to Earth structure while incorporating full-wave dynamics. Second, we adapt the tomographic framework and associated kernels for splitting intensity measurements to a specific tectonic setting (a 2-D subduction zone); this serves the important purpose of reducing the complexity of an ill-determined problem. Third, we allow heterogeneous background models for the kernel calculations.

Most literature on finite-frequency tomography deals with quasi-homogeneous background models, leading to geometrically simple kernels. In realistic heterogeneity, kernels can be more complicated and need not be 'self-similar' (in the sense that kernels at different frequencies are not merely scaled versions of one another—see also De Hoop *et al.* 2006). The use of background models with realistic heterogeneity is critical to our goal of identifying models of anisotropy beneath southwestern Japan that satisfy constraints from both shear wave splitting and geodynamic modelling.

The approach presented here also complements tomographic studies of anisotropy in the mantle wedge by Abt and Fischer (personal communication). They propose a method for shear wave splitting tomography based on the Silver & Chan (1991) measurement method applied to high-frequency local *S* phases from slab earthquakes. The application of their method is limited to regions with abundant deep seismicity and does not take into account finite frequency effects (which are likely to be small for their local *S* data set). However, their method has the advantage that the target region is—by design—confined to the mantle wedge region, whereas our ability to localize mantle wedge anisotropy depends more critically on station and source geometry.

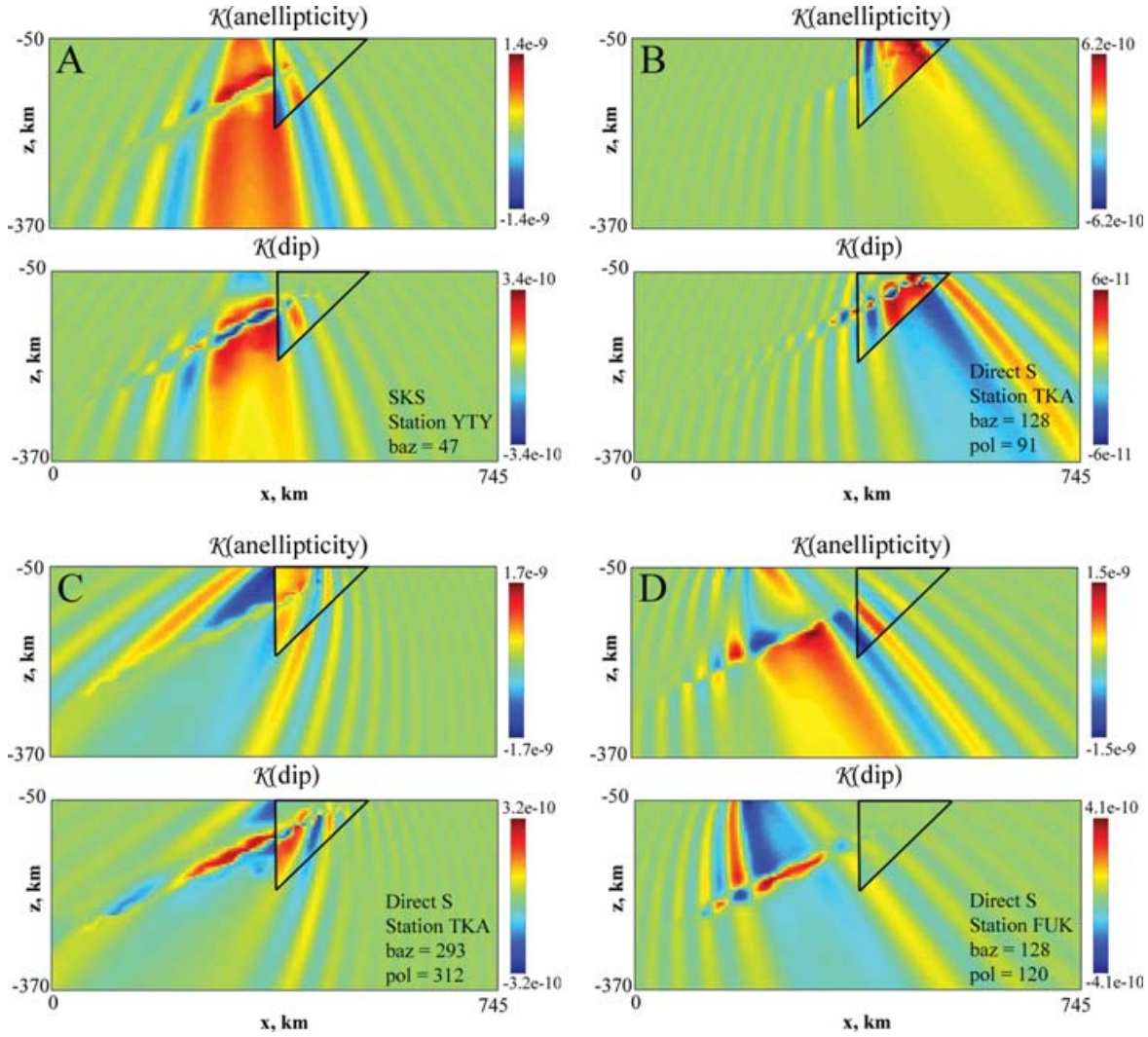

Figure 6. (a–d) Sensitivity kernel examples for the same four event-station pairs as in Fig. 4, but here the sensitivities are computed with respect to the heterogenous, anisotropic background model shown in Fig. 3. All sensitivities are given in s m^{-2}. Black lines outline the region of the mantle wedge that is dominated by B-type olivine fabric in the background model. For the kernel computation, the starting model, calculated on the coarse grid (21.25 × 21.25 km) used in the flow modelling framework (see Long *et al.* 2007), is interpolated (cubic interpolation) to a finer grid spacing (∼4 km).

Favier *et al.* (2004) evaluated so-called near-field contributions to finite-frequency splitting intensity kernels and showed that at shallow depths, ignoring the near-field contributions can introduce errors in the kernel computations. Clearly, in our asymptotic expansions the near-field contributions are ignored, but we expect the errors thus induced to be quite small for our data set. Most of the data of Long & Van der Hilst (2005a) are associated with direct teleseismic *S* phases with periods of ∼8 s. Favier *et al.* demonstrated that for such periods the near-field effects are confined to shallow depths (<25 km). Since we do not attempt to model anisotropy shallower than 50 km, we do not expect near-field effects to be important here. Also for *SK*(*K*)*S* phases, with characteristic periods of ∼10 s, we expect that near-field effects are small.

7 SUMMARY

In this paper we have described a theoretical framework for the computation of finite-frequency sensitivity kernels for wave equation shear wave splitting intensity tomography. The theoretical development for splitting intensity tomography mirrors that of De Hoop & Van der Hilst (2005) and De Hoop *et al.* (2006) for transmission and reflection tomography, respectively. We use the Born approximation for a 2.5-D anisotropic medium to derive sensitivity kernels for the dip of the symmetry axis and the strength of anisotropy in the upper mantle. We have computed example kernels for several event-station pairs represented in our teleseismic shear wave splitting data set for southwestern Japan. We compute kernels for direct teleseismic *S* and *SK*(*K*)*S* arrivals both with respect to a homogenous background model with a single layer of horizontal anisotropy and with respect to a heterogeneous, anisotropic background model obtained from a numerical modelling study of deformation beneath the Ryukyu arc (Long *et al.* 2007). Consistent with De Hoop *et al.* (2006), we find a profound influence of the starting

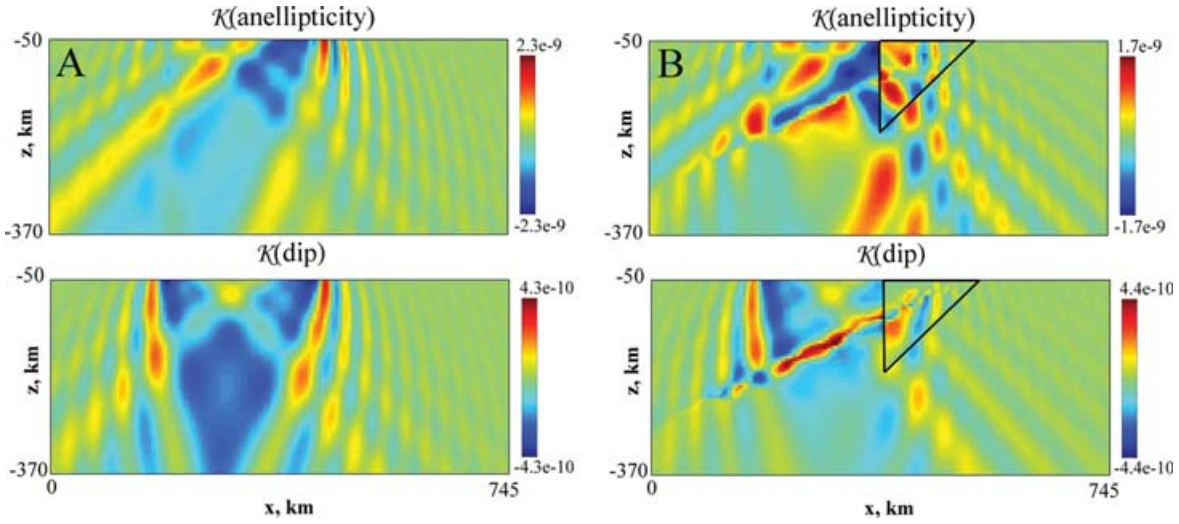

Figure 7. Sensitivity kernels for two direct *S* arrivals in the splitting data set at different *F*-net stations are shown, illustrating the localization of the anisotropic signal. (a–b). Sensitivity kernels for two direct S arrivals at stations FUK and TKA calculated for a homogenous background model. (c–d). Kernels for the same two arrivals calculated in a heterogenous background. Black lines outline the region of the mantle wedge that is dominated by B-type olivine fabric in the background model.

model on the form of the sensitivity kernels. Indeed, the suite of kernel computations shown here underscores the importance of using realistic reference models in kernel computations for finite-frequency tomographic inversions. In a companion paper to the present study (Long *et al.* in preparation) we describe the application of the wave equation splitting intensity tomography method to the Long & Van der Hilst (2005a) data set and establish a framework for integrating constraints from tomography and from numerical models of flow and deformation in the upper mantle beneath southwestern Japan. In this concept, flow modelling is used to regularize the tomographic inversion: in regions with good resolution the result from tomography is used to constrain the flow model; in turn, the flow model is used to interpolate between (or extrapolate across) regions where anisotropic structure is poorly resolved by the seismic data.

ACKNOWLEDGMENTS

We acknowledge the Japanese National Research Institute for Earth Science and Disaster Prevention (NIED) as the source for the data used in this study and thank them for making *F*-net data available and easily accessible. We thank Sebastien Chevrot for useful discussions regarding the splitting intensity metric and sensitivity kernel computations, and David Abt and Vadim Levin for discussions regarding different approaches to shear wave splitting tomography. Insightful comments by Editor Thorsten Becker, Sebastien Chevrot, and an anonymous reviewer greatly improved the clarity and presentation of the manuscript. This work was supported by NSF grant EAR-0337697.

REFERENCES

Aki, K. & Richards, P.G., 2002. *Quantitative Seismology,* University Science Books, Sausalito, CA.

Anderson, M.L., Zandt, G., Triep, E., Fouch, M. & Beck, S., 2004. Anisotropy and mantle flow in the Chile-Argentina subduction zone from shear wave splitting analysis, *Geophys. Res. Lett.,* **31,** doi:10.1029/2004GL020906.

Ando, M., Ishikawa, Y. & Yamazaki, F., 1983. Shear wave polarization anisotropy in the upper mantle beneath Honshu, Japan, *J. geophys. Res.,* **88,** 5850–5864.

Becker, T.W., Chevrot, S., Schulte-Pelkum, V. & Blackman, D.K., 2006. Statistical properties of seismic anisotropy predicted by upper mantle geodynamic models, *J. geophys. Res.,* **111,** doi:10.1029/2005JB004095.

Ben-Menahem, A., Gibson, R.L. & Sena, A.G., 1991. Green's tensor and radiation patterns of point sources in general anisotropic inhomogenous elastic media, *Geophys. J. Int.,* **197,** 297–308.

Bowman, J.R. & Ando, M., 1987. Shear-wave splitting in the upper-mantle wedge above the Tonga subduction zone, *Geophys. J. R. astr. Soc.,* **88,** 25–41.

Browaeys, J.T. & Chevrot, S., 2004. Decomposition of the elastic tensor and geophysical applications, *Geophys. J. Int.,* **159,** 667–678.

Burridge, R., De Hoop, M.V., Miller, D. & Spencer, C., 1998. Multiparameter inversion in anisotropic elastic media, *Geophys. J. Int.,* **134,** 757–777.

Červený, V., 2001. *Seismic Ray Theory,* Cambridge University Press, Cambridge.

Chapman, C.H. & Pratt, R.G., 1992. Traveltime tomography in anisotropic media – I. Theory, *Geophys. J. Int.,* **109,** 1–19.

Chevrot, S., 2000. Multichannel analysis of shear wave splitting, *J. geophys. Res.,* **105,** 21 579–21 590.

Chevrot, S., 2006. Finite-frequency vectorial tomography: a new method for high-resolution imaging of upper mantle anisotropy, *Geophys. J. Int.,* **165,** 641–657.

Chevrot, S. & Van Der Hilst, R.D., 2003. On the effects of a dipping axis of symmetry on shear wave splitting measurements in a transversely isotropic medium, *Geophys. J. Int.,* **152,** 497–505.

Chevrot, S., Favier, N. & Komatitsch, D., 2004. Shear wave splitting in three-dimensional anisotropic media, *Geophys. J. Int.,* **159,** 711–720.

Christensen, N.I., 1984. The magnitude, symmetry and origin of upper mantle anisotropy based on fabric analyses of ultramafic tectonites, *Geophys. J. R. astr. Soc.,* **76,** 89–111.

Dahlen, F.A., Hung, S.-H. & Nolet, G., 2000. Fréchet kernels for finite-frequency traveltimes – I. Theory, *Geophys. J. Int.,* **141,** 157–174.

De Hoop, M.V. & Van der Hilst, R.D., 2005a. On sensitivity kernels for 'wave-equation' transmission tomography, *Geophys. J. Int.,* **160,** 621–633.

De Hoop, M.V. & Van der Hilst, R.D., 2005b. Reply to comment by F. A. Dahlen and G. Nolet on 'On sensitivity kernels for 'wave-equation' transmission tomography, *Geophys. J. Int.,* **163,** 952–955.

De Hoop, M.V., Spencer, C. & Burridge, R., 1999. The resolving power of seismic amplitude data: an anisotropic inversion/migration approach, *Geophysics.,* **64,** 852–873.

De Hoop, M.V., Van der Hilst, R.D. & Shen, P., 2006. Wave-equation reflection tomography: annihilators and sensitivity kernels, *Geophys. J. Int.,* **167,** 1332–1352.

Esmersoy, C., 1990. Split-shear wave inversion for fracture evaluation, *Soc. Expl. Geophys. Ann. Internat. Mtg.,* **60,** 1400–1403.

Farra, V., 1989. Ray perturbation theory for heterogeneous hexagonal anisotropic media, *Geophys. J. R. astr. Soc.,* **99,** 723–737.

Farra, V., 2001. High order perturbations of the phase velocity and polarization of *q*P and *q*S waves in anisotropic media, *Geophys. J. Int.,* **147,** 93–104.

Favier, N. & Chevrot, S., 2003. Sensitivity kernels for shear wave splitting in transverse isotropic media, *Geophys. J. Int.,* **153,** 213–228.

Favier, N., Chevrot, S. & Komatitsch, D., 2004. Near-field influence on shear wave splitting and traveltime sensitivity kernels, *Geophys. J. Int.,* **156,** 467–482.

Fischer, K.M., Fouch, M.J., Wiens, D.A. & Boettcher, M. S., 1998. Anisotropy and flow in Pacific subduction zone back-arcs, *Pure appl. Geophys.,* **151,** 463–475.

Foss, S.-K., de Hoop, M.V. & Ursin, B., 2005. Linearized 2.5-dimensional parameter imaging inversion in anisotropic elastic media, *Geophys. J. Int.,* **161,** 722–738.

Fouch, M.J. & Fischer, K.M., 1996. Mantle anisotropy beneath northwest Pacific subduction zones, *J. geophys. Res.,* **101,** 15 987–16 002.

Fukao, Y., 1984. Evidence from core-reflected shear waves for anisotropy in the Earth's mantle, *Nature,* **309,** 695–698.

Hall, C., Fischer, K.M., Parmentier, E. & Blackman, D.K., 2000. The influence of plate motions on three-dimensional black are mantle flow and shear wave splitting. *J. geophys. Res.,* **105,** 28 009–28 033.

Hess, H.H., 1964. Seismic anisotropy of the uppermost mantle under oceans, *Nature,* **203,** 629–630.

Hung, S.-H., Dahlen, F.A. & Nolet, G., 2000. Fréchet kernels for finite-frequency traveltimes – II. Examples, *Geophys. J. Int.,* **141,** 175–203.

Ismail, W.B., & Mainprice, D., 1998. An olivine fabric database: an overview of upper mantle fabrics and seismic anisotropy, *Tectonophysics,* **296,** 145–157.

Jech, J. & Pšenčík, I., 1989. First-order perturbation method for anisotropic media, *Geophys. J. Int.,* **99,** 369–376.

Jung, H. & Karato, S.-I., 2001. Water-induced fabric transitions in olivine, *Science,* **293,** 1460–1463.

Karato, S.-I., 2003. Mapping water content in the upper mantle, in *Inside the Subduction Factory,* **Vol. 138**, pp. 135–152, ed. Eiler, J.M., Am. Geophys. Union. Geophys. Monogr. Ser.

Kaminski, É, & Ribe, N.M., 2002. Timescales for the evolution of seismic anisotropy in mantle flow, *Geochem. Geophys. Geosyst.,* **3,** doi:10.1029/2001GC000222.

Kennett, B.L.N., Engdahl, E.R. & Buland, R., 1995. Constraints on seismic velocities in the Earth from travel times, *Geophys. J. Int.,* **122,** 108–124.

Kneller, E.A., van Keken, P.E., Karato, S.-I. & Park, J., 2005. B-type olivine fabric in the mantle wedge: insights from high-resolution non-Newtonian subduction zone models, *Earth planet. Sci. Lett.,* **237,** 781–797.

Kosarev, G.L., Makeyeva, L.I., Savarensky, Ye.F. & Chesnokov, Ye. M., 1979. Influence of anisotropy under a seismograph station on the records of body waves, *Izvestiya, Phys. Solid Earth.,* **15,** 102–110.

Lassak, T.M., Fouch, M.J., Hall, C.E. & Kaminski, É., 2006. Seismic characterization of mantle flow in subduction systems: can we resolve a hydrated mantle wedge?, *Earth planet. Sci. Lett.,* **243,** 632–649.

Levin, V., Menke, W. & Park, J., 1999. Shear wave splitting in the Appalachians and the Urals: a case for multilayered anisotropy, *J. geophys. Res.,* **104,** 17 975–17 993.

Long, M.D. & Van Der Hilst, R.D., 2005a. Upper mantle anisotropy beneath Japan from shear wave splitting, *Phys. Earth planet. Inter.,* **151,** 206–222.

Long, M.D. & Van Der Hilst, R.D., 2005b. Estimating shear-wave splitting parameters from broadband recordings in Japan: a comparison of three methods, *Bull. seism. Soc. Am.,* **95,** 1346–1358.

Long, M.D. & Van Der Hilst, R.D., 2006. Shear wave splitting from local events beneath the Ryukyu Arc: Trench-parallel anisotropy in the mantle wedge, *Phys. Earth planet. Inter.,* **155,** 300–312.

Long, M.D., Hager, B.H., De Hoop, M.V. & Van Der Hilst, R.D., 2007. Two-dimensional modeling of subduction zone anisotropy with application to southwestern Japan, *Geophys. J. Int.,* **170,** 839–856.

Luo, Y. & Schuster, G.T., 1991. Wave-equation travel time inversion, *Geophysics,* **56,** 645–653.

MacBeth, C., 1991. Inversion for subsurface anisotropy using estimates of shear-wave splitting, *Geophys. J. Int.*, **107,** 585–595.

McKenzie, D., 1979. Finite deformation during fluid flow, *Geophys. J. R. astr. Soc.,* **58,** 689–715.

Mensch, T. & Rasolofosaon, P., 1997. Elastic-wave velocities in anisotropic media of arbitrary symmetry—generalization of Thomsen's parameters ϵ, δ, and γ, *Geophys. J. Int.,* **128,** 43–64.

Mizukami, T., Wallis, S.R. & Yamamoto, J., 2004. Natural examples of olivine lattice preferred orientation patterns with a flow-normal a-axis maximum, *Nature,* **427,** 432–436.

Montagner, J.-P. & Kennett, B.L.N., 1995. How to reconcile body-wave and normal-mode reference Earth models?, *Geophys. J. Int.,* **125,** 229–248.

Okaya, D.A. & McEvilly, T.V., 2003. Elastic wave propagation in anisotropic crustal material possessing arbitrary internal tilt, *Geophys. J. Int.,* **153,** 344–358.

Park, J. & Levin, V., 2002. Seismic anisotropy: tracing plate dynamics in the mantle, *Science,* **296,** 485–489.

Pozgay, S.H., Wiens, D.A., Conder, J.A., Shiobara, H. & Sugioka, H., 2007. Complex mantle flow in the Mariana subduction system: evidence from shear wave splitting, *Geophys. J. Int.,* **170,** 371–386.

Ryberg, T., Rümpker, G., Haberland, C., Stromeyer, D. & Weber, M., 2005. Simultaneous inversion of shear wave splitting observations from seismic arrays, *J. geophys. Res.,* **110,** doi:10.1029/2004JB003303.

Savage, M.K., 1999. Seismic anisotropy and mantle deformation: what have we learned from shear wave splitting?, *Rev. Geophys.,* **37,** 65–106.

Schoenberg, M.A. & de Hoop, M.V., 2000. Approximate dispersion relations for qP-qSV-waves in transversely isotropic media, *Geophysics,* **65,** 919–933.

Šílený, J. & Plomerová, J., 1996. Inversion of shear-wave splitting parameters to retrieve three-dimensional orientation of anisotropy in continental lithosphere, *Phys. Earth planet. Inter.,* **95,** 277–292.

Silver, P.G., 1996. Seismic anisotropy beneath the continents: probing the depths of geology, *Annu. Rev. Earth planet. Sci.,* **24,** 385–432.

Silver, P.G. & Chan, W.W., 1988. Implications for continental structure and evolution from seismic anisotropy, *Nature.,* **335,** 34–39.

Silver, P.G. & Chan, W.W., 1991. Shear wave splitting and subcontinental mantle deformation, *J. geophys. Res.,* **96,** 16 429–16 454.

Silver, P.G. & Savage, M.K., 1994. The interpretation of shear-wave splitting parameters in the presence of two anisotropic layers, *Geophys. J. Int.,* **119,** 949–693.

Skemer, P., Katayama, I. & Karato, S.-I., 2006. Deformation fabrics of the Cima di Gagnone peridotite massif, Central Alps, Switzerland: evidence of deformation at low temperatures in the presence of water, *Contrib. Mineral. Petrol.,* **152,** 43–51.

Smith, G.P., Wiens, D.A., Fischer, K.M., Dorman, L.M., Webb, S.C. & Hildebrand, J.A., 2001. A complex pattern of mantle flow in the Lau Backarc, *Science,* **292,** 713–716.

Thomsen, L., 1986. Weak elastic anisotropy, *Geophysics,* **51,** 1954–1966.

Tromp, J., Tape, C. & Liu, Q., 2005. Seismic tomography, adjoint methods, time reversal, and banana-donut kernels, *Geophys. J. Int.,* **160,** 195–216.

Wiens, D.A. & Smith, G.P., 2003. Seismological constraints on structure and flow patterns within the mantle wedge, in *Inside the Subduction Factory,* Vol. 138, pp. 59–81, ed. Eiler, J.M., Am. Geophys. Union. Geophys. Monogr. Ser.

Yang, M., Elkibbi, M. & Rial, J.A., 2005. An inversion scheme to model subsurface fracture systems using shear wave splitting polarization and delay time observations simultaneously, *Geophys. J. Int.,* **160,** 939–947.

Zhang, S. & Karato, S.-I., 1995. Lattice preferred orientation of olivine aggregates deformed in simple shear, *Nature,* **415,** 777–780.

Zheng, X., 2004. Inversion for elastic parameters in weakly anisotropic media, *Geophys. J. Int.,* **159,** 1077–1089.

Zhu, J. & Dorman, J., 2000. Two-dimensional, three-component wave propagation in a transversely isotropic medium with arbitrary-orientation-finite-element modeling, *Geophysics,* **65,** 934–942.

APPENDIX A: TABLE OF SYMBOLS

Symbol	Found near	Meaning
S	(1)	Splitting intensity
$\mathbf{x}^s$ ($\mathbf{x}^r$)	(1)	Source (receiver) position
$N_{s,r}$	(1)	Normalized radial component energy
C	(1)	Cross-correlation in time
u	(1)	Displacement field
^{R}	(1)	Superscript denoting radial component
^{T}	(1)	Superscript denoting transverse component
t	(1)	Time
u_0	(3)	Unperturbed field
δu	(3)	Perturbed field
$(\delta)c_{ijkl}$	(3)	(Perturbed) elasticity tensor
$^R h_0$, $^T h_0$	(3)	Radial, transverse initial polarization vector
$\mathcal{K}$	(3)	Sensitivity kernel
H	(5)	Linear integral operator acting on $\delta\mathbf{c}$
F	(6)	Forward modelling operator
ε	(7)	Misfit functional
F^*	(7)	Adjoint of F
$\mathbf{I}$	(7)	Image of elasticity tensor update
$\rho(\mathbf{x})$	(9)	Mass density
$f^s(\mathbf{x})$	(9)	Equivalent body force
w^*	(9)	Adjoint field
$W^s(t)$	(10)	Source function
ω	(11)	Angular frequency
G	(11)	Green's function
T	(11)	Traveltime along ray segment
$\mathbf{h}$	(11)	Unit polarization vector
A	(12)	Amplitude
$\mathbf{M}$	(13)	Moment tensor
v^s, v	(14)	Phase velocities evaluated in slowness direction
$\kappa(\mathbf{x}, \mathbf{x}^s)$	(14)	KMAH index (counts caustics between $\mathbf{x}$ and $\mathbf{x}^s$)
$\lvert\det \mathbf{Q}_2(\mathbf{x}, \mathbf{x}^s)\rvert^{1/2}$	(14)	Relative geometrical spreading
$\mathbf{q}$	(16)	Local phase-related coordinates
$Q_2^{\lvert\rvert(\perp)}$	(16)	In-plane (out-of-plane) geometrical spreading factor
$A^{\lvert\rvert}$	(17)	In-plane amplitude
$\mathbf{p}^{s(r)}$	(18)	Slowness vector associated w/ source (receiver) ray
β	(19)	Subscript indicating (q)SV,SH modes
α	(19)	Subscript indicating (q)SV mode
$\mathcal{L}^{\perp}_{\beta\alpha}$	(19)	Refracted out-of-plane geometrical spreading
$\mathbf{w}$	(19)	Radiation pattern matrix
θ_0	(35)	Dip parameter
ε_A	(35)	Anellipticity parameter

APPENDIX B: BEHAVIOUR OF THE SPLITTING INTENSITY AND KERNELS

In the notation of Chevrot (2000, 2006) and Chevrot *et al.* (2004), the splitting intensity S, obtained by projecting the transverse component waveform onto the radial component derivative, is written as

$$S = -2\frac{\int_{-\infty}^{\infty} -\mathrm{i}\omega u_T(\omega) u_R^{0*}(\omega)\mathrm{d}\omega}{\int_{-\infty}^{\infty} \omega^2 |u_R^{0*}(\omega)|^2 \mathrm{d}\omega}, \tag{B1}$$

which is equivalent to our expression (1). The *splitting function* refers to the dependence of the splitting intensity on the incoming polarization azimuth; the *splitting vector* then refers to the sample of the splitting function obtained at different incoming polarization azimuths for a given (limited) data set at a single seismic station.

Under certain assumptions, the average splitting parameters of the medium can be retrieved from the splitting vector. For example, if the anisotropy beneath the station is contained in a single, homogenous anisotropic layer with a horizontal axis of symmetry, then the splitting function for shear phases with vertical incidence takes the form (Chevrot 2000)

$$\mathrm{S} = \delta t \sin[2(\phi - \phi_0)], \tag{B2}$$

where ϕ is the azimuth of the fast symmetry axis, ϕ_0 the incoming polarization azimuth of the wave, and δt the delay time accumulated between the fast and slow components. A detailed comparison of the splitting intensity measure with other methods of measuring shear wave splitting parameters can be found in the appendix to Chevrot *et al.* (2004); an evaluation of the performance of different splitting measurement methods for broad-band Japanese stations is discussed in Long & Van der Hilst (2005b).

Favier & Chevrot (2003) have developed expressions that describe 2-D and 3-D Fréchet kernels for the splitting intensity in a homogenous anisotropic medium with a horizontal axis of symmetry. They parametrize the medium using two anisotropic perturbation parameters γ_{c} and γ_{s}, which are related to the anisotropic parameter γ of Thomsen (1986) and Mensch & Rasolofosaon (1997). The expressions they derive for the sensitivity kernels are in fact equivalent to framework derived above and expressed in eq. (33), although we make different assumptions about the geometry of the anisotropic medium, we restrict ourselves to the 2.5-D case, and we parametrize the anisotropic medium differently. Our expression for the sensitivity kernel in eq. (33) is a generalization of the treatment in Favier & Chevrot (2003) with the following differences in notation. They express the splitting intensity perturbation δS in the following form:

$$\delta \mathrm{S}(\mathbf{r}_0; \mathbf{r}) = -\gamma \frac{1}{4\pi\beta^2} \frac{2\omega_0}{r} F(\theta, \varphi, \alpha, \varphi_0) \frac{2\int_{-\infty}^{\infty} \omega^3 \, |u_R(\omega)|^2 \sin\left[\frac{\omega(r+z_0-z)}{\beta}\right] d\omega}{\int_{-\infty}^{\infty} \omega^2 \, |u_R(\omega)|^2 \, d\omega}. \tag{B3}$$

We, following from eq. (33), express the splitting intensity due to an elastic perturbation $\delta\mathbf{c}$ in the form

$$\begin{aligned} \delta \mathrm{S}(\mathbf{x}^s, \mathbf{x}^r) = \int \mathcal{K}(\mathbf{x}^s, \mathbf{x}, \mathbf{x}^r) \simeq \left[\int \omega^2 \, |W^s(\omega)|^2 \, d\omega\right]^{-1} \sum_{\beta=(\mathrm{q})\mathrm{SV},(\mathrm{q})\mathrm{SH}} {}^T h_{0,m}(\mathbf{x}^r)^{\beta} h^r_m(\mathbf{x}^r) \\ \times (-)\sqrt{\frac{\mathrm{i}}{2\pi}} \int \mathrm{i}\omega^{5/2} \rho(\mathbf{x}) \frac{[\rho(\mathbf{x}^r)^{\alpha} v^s(\mathbf{x}^r)]^{1/2}}{[\rho(\mathbf{x})^{\alpha} v^s(\mathbf{x})]^{1/2}} A^{||}_{\beta}(\mathbf{x}^r, \mathbf{x}) \\ \times \, |W^s(\omega)|^2 \, exp\left[i\omega(T_{\beta\alpha}(\mathbf{x}^r, \mathbf{x}, \mathbf{x}^s) - T_0(\mathbf{x}^r, \mathbf{x}^s)\right] d\omega \mathbf{w}^T_{\beta\alpha}(\mathbf{x}^r, \mathbf{x}, \mathbf{x}^s) \delta\mathbf{c}(\mathbf{x}) \mathrm{d}\mathbf{x}. \end{aligned} \tag{B4}$$

The differences in notation are as follows: we denote the source and scatterer position, respectively, with $\mathbf{x}^s$ and $\mathbf{x}$; their convention utilizes $\mathbf{r}_0$ and $\mathbf{r}$. Our expression for the radiation patterns, $\mathbf{w}^T_{\beta\alpha}(\mathbf{x}^r, \mathbf{x}, \mathbf{x}^s)$, is equivalent to their function $F(\theta,\phi,\alpha,\phi_0)$ normalized by β^2, the square of the isotropic shear wave speed. Their work assumes that the perturbation in anisotropy is completely described by a perturbation in c_{44}: therefore, our $\delta\boldsymbol{c}$ is equivalent to their $\gamma = \frac{-\delta c_{44}}{c_{44}}$, multiplied by $\beta^2\rho$ (because $\beta = \sqrt{\frac{c_{44}}{\rho}}$). We write the geometrical spreading as $\rho(\mathbf{x}) A^{||}_{\beta}(\mathbf{x}^r, \mathbf{x})$; due to the homogenous model and resulting ray path geometry used in Favier & Chevrot (2003), their expression for the geometrical spreading simplifies to $1/4\pi\beta r$. The ratio of densities and isotropic velocities $[\rho(\mathbf{x}^r)^{\alpha} v^s(\mathbf{x}^r)]^{1/2}/[\rho(\mathbf{x})^{\alpha} v^s(\mathbf{x})]^{1/2}$ that appears in our kernel expressions simplifies to 1 in the case of a homogeneous layer, as assumed in Favier & Chevrot (2003). Finally, we write the traveltime difference between the perturbed and unperturbed rays as $T_{\beta\alpha}(\mathbf{x}^r, \mathbf{x}, \mathbf{x}^s) - T_0(\mathbf{x}^r, \mathbf{x}^s)$, while for their geometry this expression can be written simply as $\frac{r+z_0-z}{\beta}$. The only substantial difference between our expression (33) and their expression (33) is the extra $\omega^{3/2}$ factor in the frequency integral that appears in our 2.5-D case. The differences between 2-D and 3-D kernels are discussed in the appendix to Favier & Chevrot (2003); they also note the $\omega^{5/2}$ frequency dependence in the integral. In their approach, this $\omega^{5/2}$ term means that the integral can no longer be evaluated analytically and numerical integration is needed; in our computational approach, we have assumed a narrow frequency band and have taken the frequency terms outside the integral.

APPENDIX C: DEFINITION, ROTATION, AND PERTURBATION OF STIFFNESS TENSOR

Here we discuss the definition of the stiffness tensor for TI medium, its rotation in the (x_1-x_3) or (x_2-x_3) plane, and its perturbation to calculate the derivatives used in the kernel computation. In the background anisotropic model, we consider cases between isotropic mantle (see e.g. Browaeys & Chevrot 2004) (2 independent elastic parameters—this case corresponds to finite strains of $\gamma = 0$ in our flow models) and the transversely isotropic mantle (TIM) model of Chevrot & Van der Hilst (2003) (5 parameters—this case corresponds to $\gamma = 3$); the intermediate solutions (e.g. orthorhombic symmetry) can involve more parameters, but we recall that with the 2.5-D approximation we can

constrain, at most, 7 parameters. The elastic tensor for a transversely isotropic medium can be written in the form (e.g. Thomsen 1986):

$$C{=}c_{ij} = \begin{bmatrix} c_{11} & c_{11}-2c_{66} & c_{13} & 0 & 0 & 0 \\ c_{11}-2c_{66} & c_{11} & c_{13} & 0 & 0 & 0 \\ c_{13} & c_{13} & c_{33} & 0 & 0 & 0 \\ 0 & 0 & 0 & c_{55} & 0 & 0 \\ 0 & 0 & 0 & 0 & c_{55} & 0 \\ 0 & 0 & 0 & 0 & 0 & c_{66} \end{bmatrix}. \tag{C1}$$

Here we follow the convention of contracting the fourth-rank elasticity tensor c_{ijkl} into a 6×6 matrix (Voigt notation). Following Zhu & Dorman (2000) and Okaya & McEvilly (2003), we rotate this tensor in the $(x_1{-}x_3)$ or $(x_2{-}x_3)$ plane, depending on the strike of the symmetry axis. For $\alpha = 0$ (that is, in the B-type fabric regime), the rotation matrix is given by

$$R_1 = \begin{bmatrix} \cos^2\theta_0 & 0 & \sin^2\theta_0 & 0 & 2\sin\theta_0\cos\theta_0 & 0 \\ 0 & 1 & 0 & 0 & 0 & 0 \\ \sin^2\theta_0 & 0 & \cos^2\theta_0 & 0 & -2\cos\theta_0\sin\theta_0 & 0 \\ 0 & 0 & 0 & \cos\theta_0 & 0 & -\sin\theta_0 \\ -\cos\theta_0\sin\theta_0 & 0 & \cos\theta_0\sin\theta_0 & 0 & \cos^2\theta_0-\sin^2\theta_0 & 0 \\ 0 & 0 & 0 & \sin\theta_0 & 0 & \cos\theta_0 \end{bmatrix} \tag{C2}$$

and the rotated elastic constant matrix is given by RCR^T. After rotation, the 7 independent elastic constants that we can constrain with the 2.5-D geometry (Section 4.3) can be collected into vector $\mathbf{c}'$:

$$\mathbf{c}' = \begin{bmatrix} c'_{11} \\ c'_{13} \\ c'_{33} \\ c'_{44} \\ c'_{15} \\ c'_{35} \\ c'_{55} \end{bmatrix}. \tag{C3}$$

The radiation pattern matrix then also reduces to seven independent entries (see eq. 27).

We obtain the following expressions for the rotated elastic parameters:

$$c'_{11} = (2c_{13}+4c_{55})\sin^2\theta_0\cos^2\theta_0 + c_{11}\cos^4\theta_0 + c_{33}\sin^4\theta_0. \tag{C4}$$

$$c'_{13} = (c_{11}+c_{33}-4c_{55})\sin^2\theta_0\cos^2\theta_0 + c_{13}\cos^4\theta_0 + c_{13}\sin^4\theta_0. \tag{C5}$$

$$c'_{33} = (2c_{13}+4c_{55})\sin^2\theta_0\cos^2\theta_0 + c_{11}\sin^4\theta_0 + c_{33}\cos^4\theta_0. \tag{C6}$$

$$c'_{35} = (c_{33}-c_{13})\cos^3\theta_0\sin\theta + (c_{13}-c_{11})\sin^3\theta_0\cos\theta_0 - 2c_{55}\cos^3\theta_0\sin^3\theta_0. \tag{C7}$$

$$c'_{44} = c_{55}\cos^2\theta_0 + c_{66}\sin^2\theta_0. \tag{C8}$$

$$c'_{15} = (c_{13}-c_{11})\cos^3\theta_0\sin\theta_0 - (c_{13}+c_{33})\sin^3\theta_0\cos\theta_0 + 2c_{55}\cos^3\theta_0\sin^3\theta_0, \tag{C9}$$

$$c'_{55} = (c_{11}+c_{33}-2c_{55})\cos^2\theta_0\sin^2\theta_0 + c_{55}\cos^4\theta_0 + c_{55}\sin^4\theta_0. \tag{C10}$$

Finally, in these equations we can substitute for the elastic constants c_{11}, c_{13}, c_{33}, and c_{55} expressions in terms of the anellipticity ϵ_A, according to eq. (35). For the case where $\alpha = 90^\circ$ (fast axis is perpendicular to the trench), the process is similar but the rotation matrix R_1 is replaced by

$$R_2 = \begin{bmatrix} 0 & 1 & 0 & 0 & 0 & 0 \\ \cos^2\theta_0 & 0 & \sin^2\theta_0 & 0 & 2\cos\theta_0\sin\theta_0 & 0 \\ \sin^2\theta_0 & 0 & \cos^2\theta_0 & 0 & -2\cos\theta_0\sin\theta_0 & 0 \\ \cos\theta_0\sin\theta_0 & 0 & -\sin\theta_0\cos\theta_0 & 0 & \sin^2\theta_0\cos^2\theta_0 & 0 \\ 0 & 0 & 0 & \cos\theta_0 & 0 & -\sin\theta_0 \\ 0 & 0 & 0 & -\sin\theta_0 & 0 & -\cos\theta_0 \end{bmatrix}. \tag{C11}$$

Now we have expressed the rotated stiffness matrix as a function of the chosen anisotropic parameters θ_0 and ε_{A}. We linearize the relationships to obtain derivatives of the stiffness tensor components with respect to θ_0 and ε_{A}. We write the partial derivatives as

$$\delta c_{\varepsilon A} = \frac{\partial c}{\partial \varepsilon_{\mathrm{A}}} \delta \varepsilon_{\mathrm{A}} \tag{C12}$$

$$\delta c_{\theta} = \frac{\partial c}{\partial \theta_0} \delta \theta_0, \tag{C13}$$

where c represents a non-zero component of the stiffness tensor. The total perturbation in the stiffness tensor component can then be written as

$$\delta \mathbf{c} = \delta c_{\varepsilon A} + \delta c_{\theta} = \frac{\partial \mathbf{c}}{\partial \varepsilon_{\mathrm{A}}} \delta \varepsilon_{\mathrm{A}} + \frac{\partial \mathbf{c}}{\partial \theta_0} \delta \theta_0. \tag{C14}$$